Supporting Information

Highly Active NiCe(Fe)O_xH_y Electrocatalyst for Oxygen Evolution Reaction with Ultralow Fe Leaching

Zicong Zhang,[ab] Xiurui An,[ab] Jun Chen,[ab] Pengfei Zhang,[ac] Ying Zhang,[a] Jie Zhang,[ab] Yi Lu,[ad] Panwang Zhou,[ab] Junyuan Xu,[ad] Tingting Yao,*[ae] and Can Li,*[ab]

[a.] *State Key Laboratory of Catalysis, Dalian National Laboratory for Clean Energy, Dalian Institute of Chemical Physics, Chinese Academy of Sciences, Dalian 116023, China. E-mail: canli@dicp.ac.cn; ttyao@dicp.ac.cn*

[b.] *University of Chinese Academy of Sciences Beijing 100049, China*

[c.] *College of Chemistry, Jilin University, Changchun 130021, China*

[d.] *Laboratory of Advanced Spectro-electrochemistry and Li-ion Batteries, Dalian National Laboratory for Clean Energy, Dalian Institute of Chemical Physics, Chinese Academy of Sciences. Dalian 116023, China.*

[e.] *Center of Materials Science and Optoelectronics Engineering, University of Chinese Academy of Sciences, Beijing 100049, China*

Experimental Section

Chemicals: Ni mesh (NM) and Raney Ni (RN) mesh was purchased from Jingli Hydrogen Production Equipment Co., Ltd. Ferric nitrate nonahydrate ($Fe(NO_3)_3·9H_2O$, 98.5%), cerium(III) nitrate hexahydrate ($Ce(NO_3)_3·6H_2O$, 99.0%), potassium hydroxide (KOH, 85%), sodium hydroxide (NaOH, 90%) and ethanol (C_2H_5OH, 99.7%) were purchased from Sinopharm Chemical Reagent Co., Ltd. Nickel powder, molybdenum powder and aluminum powder (180~250 mesh) were purchased from Yangzhou Yufeng Special Mesh Belt Factory. Tetramethalammonium hydroxide pentahydrate ($C_4H_{13}NO·5H_2O$, $TMAOH·5H_2O$, 97%) was purchased from Shanghai Macklin Biochemical Co., Ltd. ^{18}O-Water ($H_2{}^{18}O$, 97 atom% ^{18}O) was purchased from Meryer (Shanghai) Chemical Technology Co., Ltd. In addition to special description, all solutions were prepared using deionized (DI) Milli-Q water (18.2 MΩ cm^{-1} at 25 °C).

Material Synthesis

Preparation of catalyst-annealed Nickel mesh (NM): NM substrate was ultrasonically cleaned in acetone, isopropanol, ethanol and deionized water for 20 min prior to use. The cleaned NM was placed in a tube furnace and kept at 150°C for 2 hours in a mixed atmosphere of H_2 and Ar. The volume ratio of H_2:Ar is 1:19. The annealed NM was prepared after cooling down to room temperature.

$NiCe(Fe)O_xH_y$ electrodes: The annealed NM was immersed into a glass beaker with 50 ml solution containing a mM $Ce(NO_3)_3$ and b mM $Fe(NO_3)_3$. The beaker was then put in a water bath which was heated to 60°C in advance. Keep the system still for 12 hours and then the resultant electrode was washed thoroughly with deionized water to remove the impurities from the solution and air dried, which was denoted as $NiCe_a(Fe_b)O_xH_y$. The OER activities of $NiCe(Fe)O_xH_y$ were optimized by changing various Ce:Fe feeding ratio and soaking time.

$NiFeO_xH_y$ electrode: The NiFe electrode was prepared with the same approach as for the synthesis of $NiCe(Fe)O_xH_y$ electrode without the addition of $Ce(NO_3)_3$.

$NiCeO_xH_y$ electrode: The NiCe electrode was prepared with the same approach as for the synthesis of $NiCe(Fe)O_xH_y$ electrode without the addition of $Fe(NO_3)_3$.

Preparation of NiMo electrode: Nickel powder, molybdenum powder and aluminum powder was mixed in a mass ratio of 3.2:0.8:1 and then deposited on the nickel mesh through plasma spraying process to obtain the NiMoAl electrode.

Pretreatment of RN and NiMo electrode: The as-received samgples were immerged into the w_t=10% KOH solution for 24 hours before used as the counter electrode in three-electrode test and as the cathode for overall water splitting.

Preparation of Fe-free KOH[1]: The Fe-free KOH was prepared for Operando Raman experiments of pure NF and pure Ni hydroxide (see below). The Fe impurities in normal KOH solutions can be removed by treating with high-purity $Ni(OH)_2$. In a clean 100 mL polypropylene centrifuge tube, 2 g of $Ni(NO_3)_2 \cdot 6H_2O$ (99.99%) was dissolved in 8 mL of ultrapure water. 20 mL of 1 M KOH solution was added to give a $Ni(OH)_2$ precipitate. The suspension was agitated and centrifuged, and the supernatant was decanted. The $Ni(OH)_2$ precipitate was washed with ultrapure water for three times by centrifugation. The solid was dispersed in 2 mL of 1 M KOH and 15 mL of DI water by centrifugation, and the supernatant was decanted. This solid was used as the Fe-absorber. The cleaning procedure involves dispersing $Ni(OH)_2$ in the KOH solution, mechanically agitated over-night, followed by at least 4 h of resting.

Preparation of Fe-free TMAOH: similar approach as for the preparation of Fe-free KOH by using TMAOH to represent KOH.

Material Characterizations

X-ray diffraction (XRD), scanning electron microscopy (SEM), High-resolution transmission electron microscopy (HRTEM), X-ray photoelectron spectroscopy (XPS), inductively coupled plasma atomic emission spectrometry (ICP-AES), energy-dispersive X-ray (EDX) and operando Raman spectroscopy were employed to analyze the samples. The phase analyses of samples were performed by XRD (Smartlab) with Cu-Kα radiation. The scan rate of 2° min^{-1} was applied to record the patterns in the range of 10°-85°. The morphologies of samples and EDX analyses were investigated by field emission SEM (Quanta 200 FEG) and TEM (JEM 2100). The XPS spectra were carried out on a Thermo Esclab 250Xi photoelectron spectroscopy with a monochromatic Al Kα X-ray radiation as the X-ray source for excitation. The binding energy of C 1s (284.8 eV) was taken as reference. The ICP-OES measurements were performed on a SHIMADZU ICPS-8100. Operando Raman spectroscopy was was performed with a confocal Raman microscope (Renishaw inVia Raman microscope) with a 40× water objective (Leica). The excitation source used was a 60 mW semiconductor laser (785 nm). To avoid sample damage, a 3 mW laser was used for measurement. The in-situ experiments were made in a three-electrode cell made of PTFE, with a quartz window at the top. Pt plate, mercury oxide electrode (Hg/HgO/OH^-, 1 M KOH) and one of prepared samples mentioned in experimental section as counter electrode, reference electrode and working electrode, respectively.

X-ray Adsorption Spectroscopy.

Samples were prepared using commercially available samples of FeOOH powder, Fe_2O_3 powder and Fe foil. Powder $NiCe_2(Fe_1)O_xH_y$ was synthesized according to the portion of material synthesis and the active layer were stripped by ultrasonic method. Powder samples were finely mixed with powder hexagonal Boron Nitride (BN) and then were pressed into disks of 13 mm diameter and ~1 mm thick pellets, which were finally sealed in a Kapton tape envelope.

The X-ray absorption fine structure (XAFS) spectra of Fe and Ni K-edge were conducted in transmission mode at the BL11B beamline of the Shanghai Synchrotron Radiation Facility, China, with the energy range of 5~20 KeV. The synchrotron beam was monochromatized using a double-crystal monochromator equipped with a Si (111) crystal to reduce the harmonic component of the monochrome beam. The XAFS spectra were analyzed using the Athena and Artemis. The K-edge EXAFS spectrum fitting (without phase correction) was performed in the R space with a k-weight of 2. The following EXAFS equation was used:

$$\chi(k) = \sum_j \frac{N_j S_0^2 F_j(k)}{kR_j^2} exp\left[- 2k^2\sigma_j^2 \right] exp\left[\frac{- 2R_j}{\lambda(k)} \right] \sin\left[2kR_j + \varphi_j(k) \right]$$

where N_j is the number of neighbours in the jth atomic shell, S_0^2 is the amplitude reduction factor; $F_j(k)$ is the effective curved-wave backscattering amplitude, R_j is the distance between the X-ray absorbing central atom and the atoms in the jth atomic shell (backscatterer), σ_j is the Debye–Waller parameter of the jth atomic shell, λ is the mean free path (Å), φ_j(k) is the phase shift.

Electrochemical Measurements

The electrochemical performances of the as-prepared catalysts were evaluated in a three-electrode system by using a Gamry Interface 5000E in 1M KOH. The as-prepared electrodes, mercury oxide electrode (Hg/HgO/OH$^-$, 1 M KOH), and Raney Ni were used as working, reference and counter electrode, respectively, for electrocatalytic measurements. The cyclic voltammetry (CV) curves were carried out at a scan rate of 2 mV s^{-1} with 90% iR-compensation. The C_{dl} values for as-prepared electrodes were determined from the cyclic voltammogram (CV) in the double layer region (without Faradaic processes) at different scan rates. The chronopotentiometric curves of electrodes were tested at specific current densities with 90% iR-compensation. Tafel slope curves were transferred by staircase voltammetry with the steady-state current taken at the end of the 60 s, 10 mV steps.

The electrochemical active surface areas (ECSAs) of the catalysts were evaluated to investgate the intrinsic catalytic activity by estimating the electrochemical double-layer capacitance (C_{dl}) in a non-faradic potential range with various scan rates (10, 30, 50, 70, and 90 mV s^{-1}) (Figure S5). From the plot of current density (the sum of absolute values of current density at 0.847 V vs. RHE) against the scan rate, the C_{dl} value was determined as the slope of a straight line. Assuming the specific capacitance of 0.04 mF cm^{-2} for an ideal flat surface, the electrochemical active surface area can be calculated by the following equation:

$$A_{\mathrm{ECSA}} = \frac{C_{dl}\,(catalyst)}{0.04\;mF\;cm^{-2}}$$

The C_{dl} of $NiCe_2(Fe_1)O_xH_y$, $NiFeO_xH_y$, $NiCeO_xH_y$ and NM electrodes are determined as 0.651, 0.616, 0.718, 0.483 mF cm^{-2}, respectively (Figure S7). The ECSA values were estimated by assuming the specific capacitance of 0.04 mF cm^{-2} for an ideal flat surface.

DEMS Test

The ^{18}O labeled lattice oxygen exchange experiments were monitored with an online differential electrochemical mass spectrometer (Hyden Analytical HPR-20 EGA). The catalyst ink was prepared by dispersing 5 mg of catalyst into the solution containing 950 μL ethanol and 50 μL Nafion (5 wt.%), followed by ultrasonication for 30 min. The catalyst inks of $NiCe_2(Fe_1)O_xH_y$ and $NiFeO_xH_y$ were dispersed on a hydrophilic carbon paper with loading capacity of 1 mg/cm^2, which were used as working electrodes in 1M $KOH/H_2{}^{18}O$. Ag/AgCl electrode and Pt mesh were used as reference electrode and counter electrode, respectively. The DEMS test was performed in 1M $KOH/H_2{}^{18}O$ solution via CA test at 1.53 V, 1.63 V and 1.73 V vs. RHE for 5 min. Meanwhile, the gaseous products including $^{32}O_2$, $^{34}O_2$ and $^{36}O_2$ were monitored by the mass spectrometer. During the electrochemical measurements, all the electrolytes were maintained under a high-purity Ar atmosphere.

The purity of commercial heavy oxygen water ($H_2{}^{18}O$) is 97% in atomic ratio for ^{18}O, with the rest 3% of ^{16}O. To prepare a 1M $KOH/H_2{}^{18}O$ solution, 1.52 g KOH was added into 30 g commercial heavy oxygen water. So there are 1.46 mol ^{18}O and 0.0722 mol ^{16}O in the 1M $KOH/H_2{}^{18}O$ electrolyte. The atomic proportion of ^{18}O in the solution is 95.28% and that of ^{16}O is 4.71%. When the OER process only undergoes AEM, the theoretical proportion of mass signal of m/z=36, 34 and 32 are 90.78%, 9.00% and 0.222%. When the $^{34}O_2/^{36}O_2$ ratio is larger than 9.91%, it is possible to undergo the single lattice oxygen oxidation mechanism (sLOM). When the $^{32}O_2/^{36}O_2$ ratio is larger than 0.245%, it is possible to undergo the double lattice oxygen oxidation mechanism (dLOM).

Computational Details

The Density Functional theory (DFT) calculations of slabs in this study were conducted using the Vienna Ab initio Simulation Package (VASP) code.[2-5] The ion core potentials were modelled following the projector augmented wave (PAW)[6, 7] approach to describe the electron−core interaction. For electron exchange-correlation, the Perdew-Burke-Ernzerhof (PBE) functional within the generalized-gradient approximation (GGA) range was applied.[8, 9] A plane wave basis set was used with a cutoff energy of 400 eV. Structural relaxations were performed until the forces on each of the atoms were below 0.02 eV Å-1. During structural optimization and the self-consistent calculations, Gamma-Pack mesh k-space sampling grids[10] of 2 × 2 × 1 were used to sample the Brillouin zone (BZ). The self-consistent calculations apply a convergence energy threshold of 10^{-6} eV. All the atoms were allowed to optimize and all the energy calculations are performed using spin polarized calculations. To treat the strongly correlated d and f orbitals of transition metal (TM) atoms, the GGA + U scheme is adopted to describe the Coulomb and exchange corrections. The difference of the correlation energy U and the exchange energy J of the 3d electrons is set to 5.5 eV, 5.3 eV, and 7.0 eV for Ni, Fe, and Ce, respectively. In contrast, the delocalized s and p electrons are treated by the standard GGA method. To better describe the dispersion interaction within water adsorption systems, vdW correction was considered by adopting the Grimme's D3 scheme.[10, 11]

The Gibbs free energy changes for the water oxidation steps using LOM mechanisms were calculated using the following Equations, respectively.[10, 11]

$$\Delta G_1 = \Delta G_{*OH+*OH} - \Delta G_{*+*OH} - eU$$

$$\Delta G_2 = \Delta G_{*OH+*O} - \Delta G_{*OH+*OH} - eU$$

$$\Delta G_3 = \Delta G_{*O-O} - \Delta G_{*OH+*O} - eU$$

$$\Delta G_4 = \Delta G_{*OO+*OH} - \Delta G_{*O-O} - eU$$

$$\Delta G_5 = \Delta G_{*+*OH} - \Delta G_{*OO+*OH}$$

Where U is the potential measured against normal hydrogen electrode (NHE) at standard condition (T = 298.15 K, P = 1 bar, pH = 0). The Gibbs free energy differences of these intermediates include zero-point energy (ZPE) and entropy corrections according to $\Delta G_i = \Delta E_i + \Delta ZPE_i - T\Delta S_i$, where the energy differences ΔE_i are calculated with respect to H_2O and H_2 (at U = 0). The theoretical overpotential is defined as the lowest potential at which all reaction steps are thermodynamically downhill.

Table S1. The changes of actual relative ratios of Ni, Fe and Ce with the feeding molar ratios of Ce/Fe in NiCe(Fe)O_xH_y detected by ICP-AES.

Ce:Fe feeding ratios	Actual relative ratios of Ni/Fe/Ce
2:1	3.48/2.59/1
1:5	8.44/8.56/1
5:1	0.34/0.71/1

Table S2. OER activities of some reported Ce containing and NiFe containing electrocatalysts in alkaline solution reported recently

Catalyst	Electrolyte	Current density (mA cm^{-2})	Overpotential (mV)	Reference
NiFeCe	**1M KOH**	**10**	**224**	**This work**
NiFeCe	**1M KOH**	**500**	**303**	**This work**
NiCeO$_x$	1M KOH	10	295	ACS Catal. 2019,9,1605−1611
Ce-NiO-E	1M KOH	10	382	Adv. Funct. Mater. 2018,28, 1706056
Ce-NiO-L	1M KOH	10	426	Adv. Funct. Mater. 2018,28, 1706056
NiCeO$_x$-Au	1M NaOH	10	279	Nature Energy 2016, 1, 1-8
Hexagonal sphericon hematite Ce-Ni	1M KOH	10	260	Adv. Mater. 2017, 29, 1703792
30%Ce-Ni-Fe-LDH	1M KOH	10	242	Energy Environ. Sci., 2020, 13, 2949--2956
FeOOH/CeO$_2$ Ni foam	1M NaOH	31	250	Adv. Mater. 2016, 28,4698–4703
Ce@NiFe-LDH	1M KOH	10	206	Adv. Energy Mater. 2021, 2101281
Amorphous Ce-NiFe	1M KOH	10	195	Adv. Funct. Mater. 2022, 32, 2204086

Table S3. Local structure parameters around Ni estimated by EXAFS analysis.

Sample	S_0^2	Bond	N	R(Å)	σ^2	R-factor(%)
$NiCe_2(Fe_1)O_xH_y$	0.70	Ni-O	6.3	1.99 ± 0.02	0.0051	0.00643
		Ni-Fe	2.8	2.88 ± 0.07	0.011	
		Ni-Ni	12.2	3.09 ± 0.02		
		Ni-Ce	2.07	3.49 ± 0.14		

N= coordination number, R=distance between absorber and backscattering atoms, σ^2=Debye-Waller factor.

Table S4: Local structure parameters around Fe estimated by EXAFS analysis.

Sample	S_0^2	Bond	N	R(Å)	σ^2	R-factor(%)
$NiCe_2(Fe_1)O_xH_y$	0.70	Fe-O	6.2	1.99 ± 0.02	0.00652	0.00582
		Fe-Fe	1.42	2.90 ± 0.08		
		Fe-Ni	4.46	3.07 ± 0.03		
		Fe-Ce	2.02	3.37 ± 0.06		

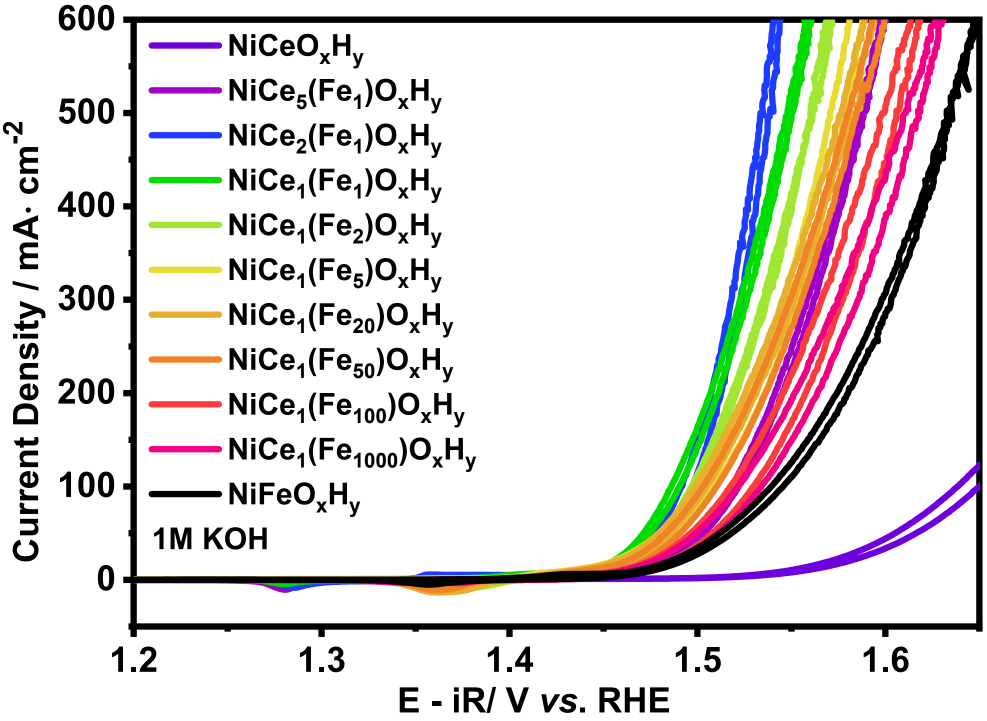

Figure S1. OER performance of NiCe(Fe)O_xH_y electrodes synthesized with different raw materials ratio of Ce:Fe at reaction time of 12h.

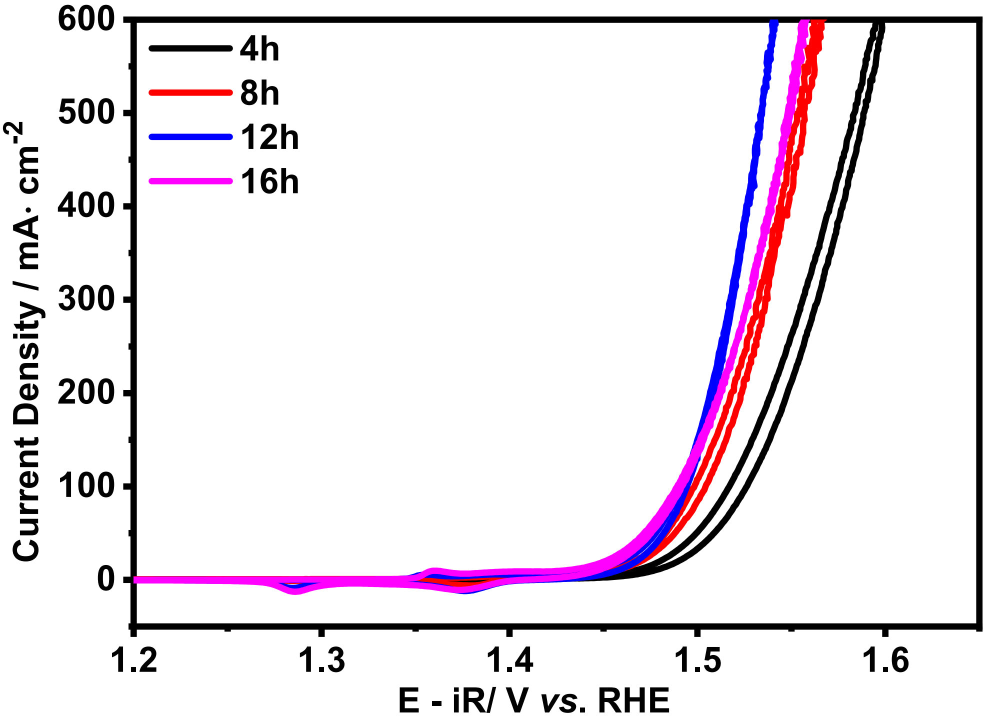

Figure S2. OER performance of NiCe(Fe)O_xH_y electrodes synthesized with different reaction time at the feeding ratio of Ce:Fe=2:1.

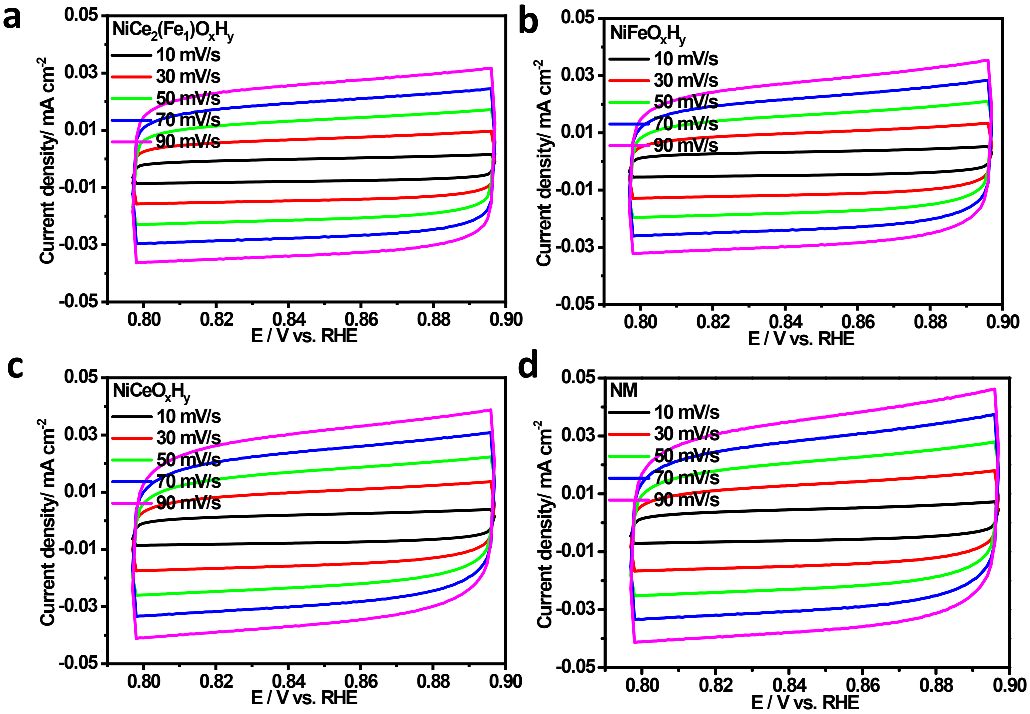

Figure S3. Cyclic voltammograms of $NiCe_2(Fe_1)O_xH_y$, $NiFeO_xH_y$, $NiCeO_xH_y$ and NM electrodes measured in O_2 saturated 1M KOH at different scan rates from 10 to 90 mV s^{-1}.

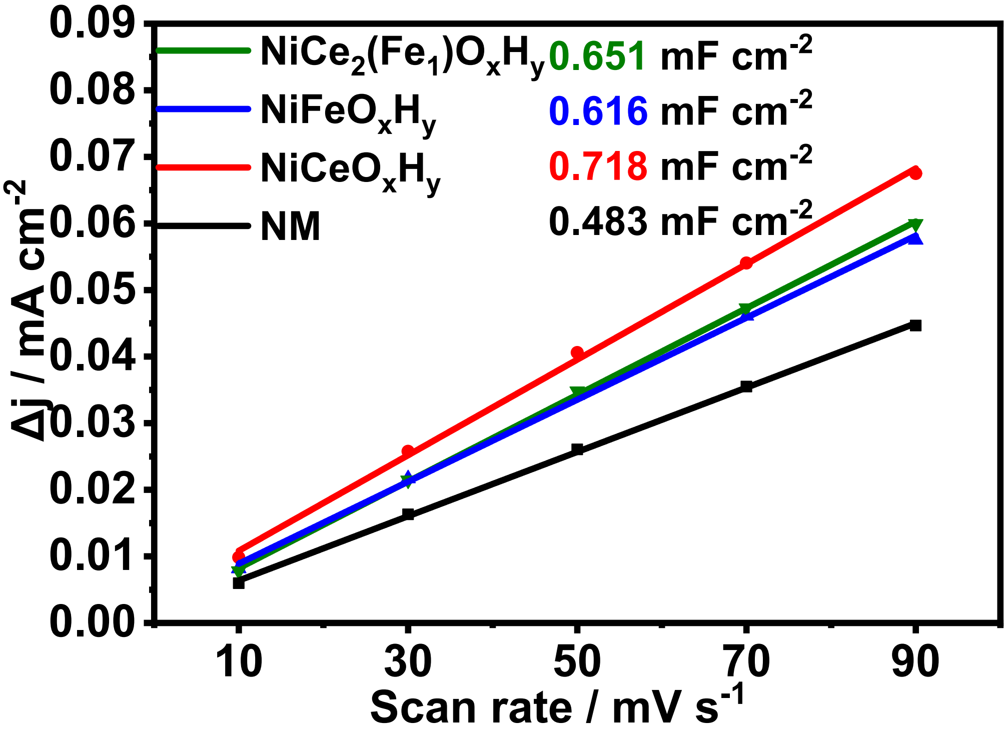

Figure S4. Fitting plots used for calculation of the double-layer capacitance (C_{dl}) for the $NiCe_2(Fe_1)O_xH_y$, $NiFeO_xH_y$, $NiCeO_xH_y$ and NM electrodes in 1M KOH.

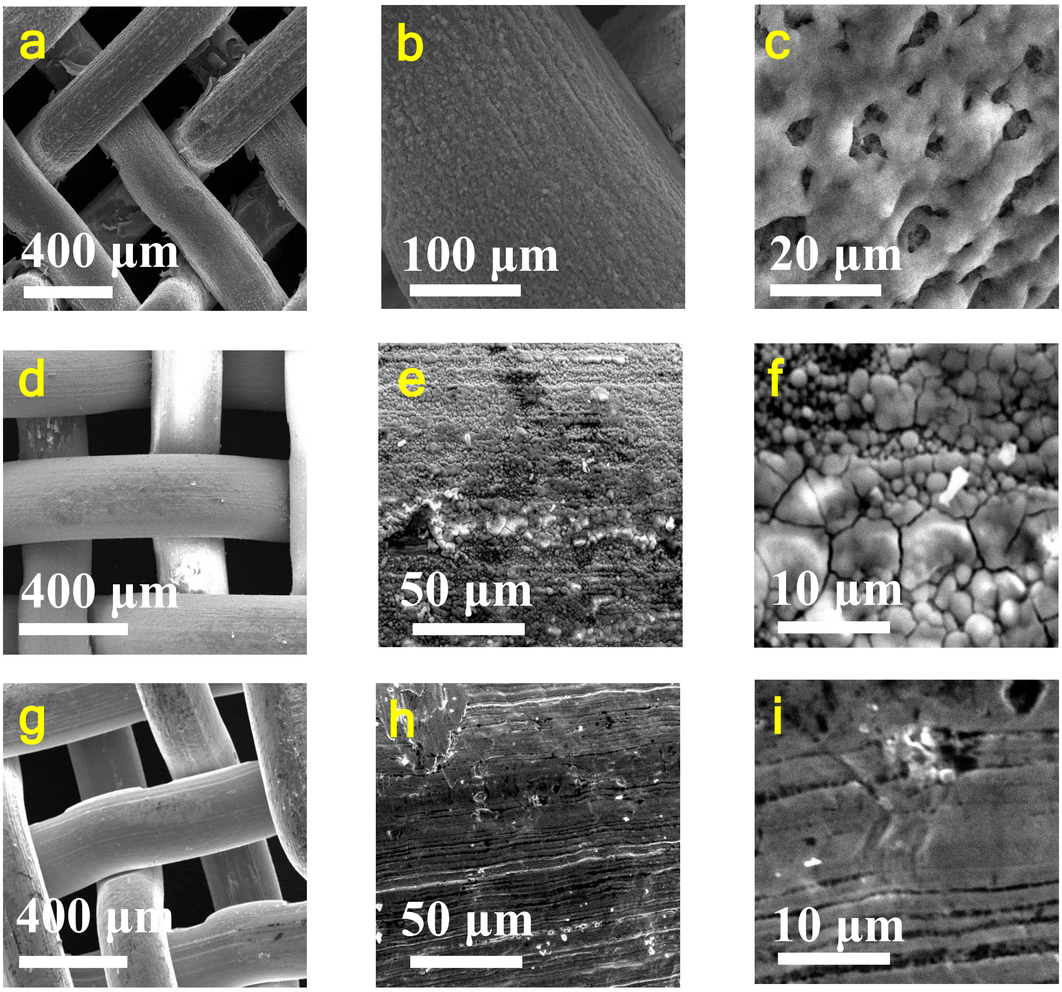

Figure S5. Scanning electron microscopy (SEM) images of (a, b, c) $NiFeO_xH_y$, (d, e, f) $NiCeO_xH_y$ and (g, h, i) NM electrodes.

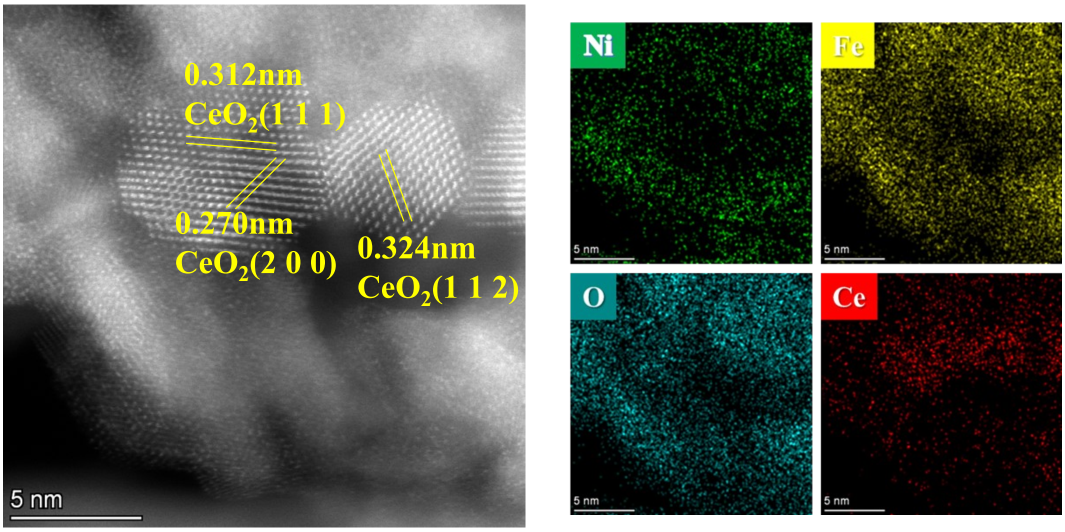

Figure S6. STEM-HAADF image and EDX elemental mappings of $NiCe_2(Fe_1)O_xH_y$ catalyst.

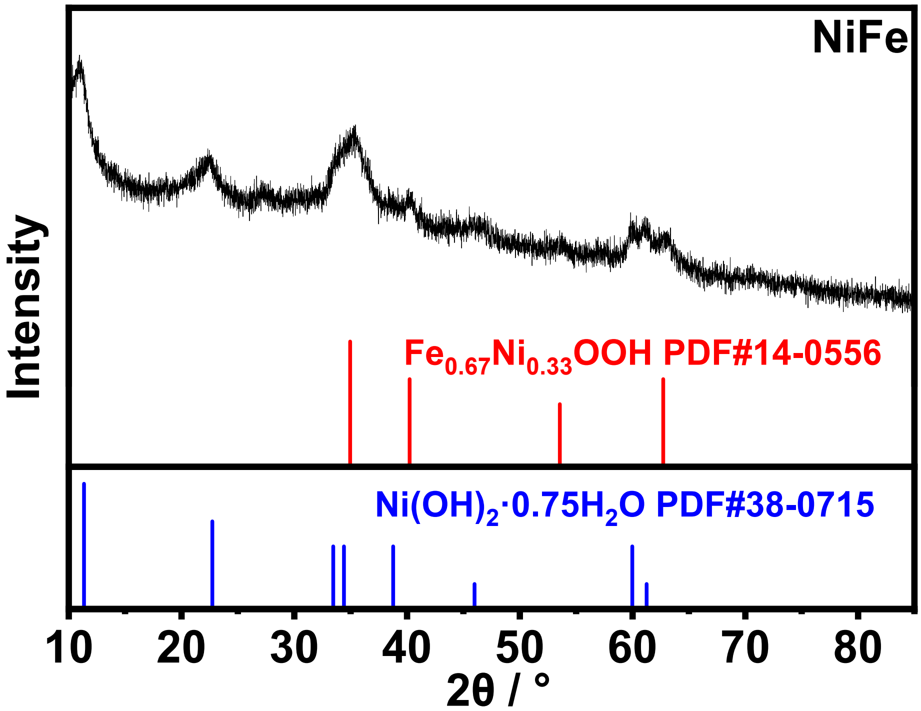

Figure S7. XRD patterns of $NiFeO_xH_y$ electrodes.

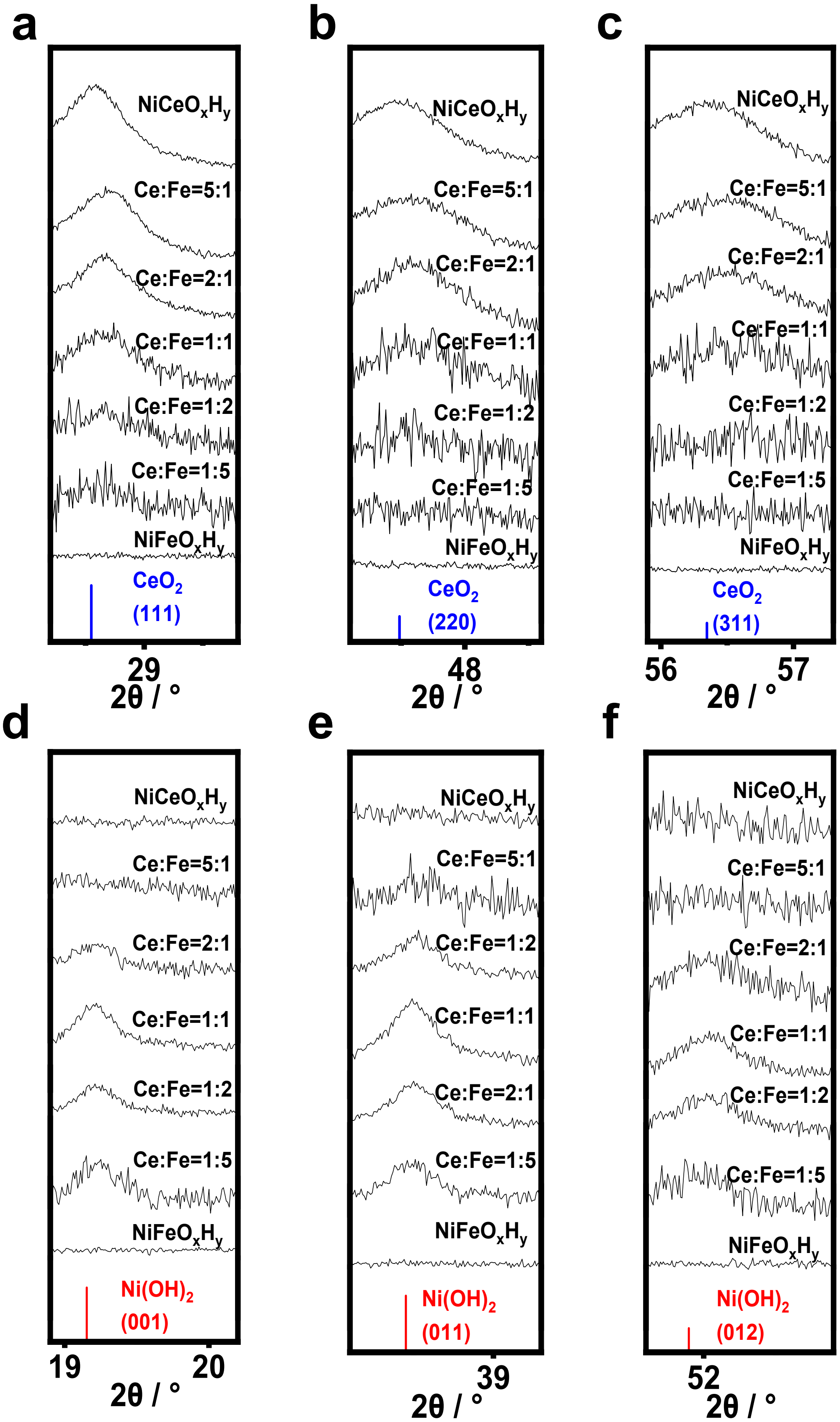

Figure S8. XRD patterns of NiCe(Fe)O$_x$H$_y$, NiFeO$_x$H$_y$ and NiCeO$_x$H$_y$ electrodes with characteristic crystal planes: (a-c) CeO$_2$ and (d-f) Ni(OH)$_2$.

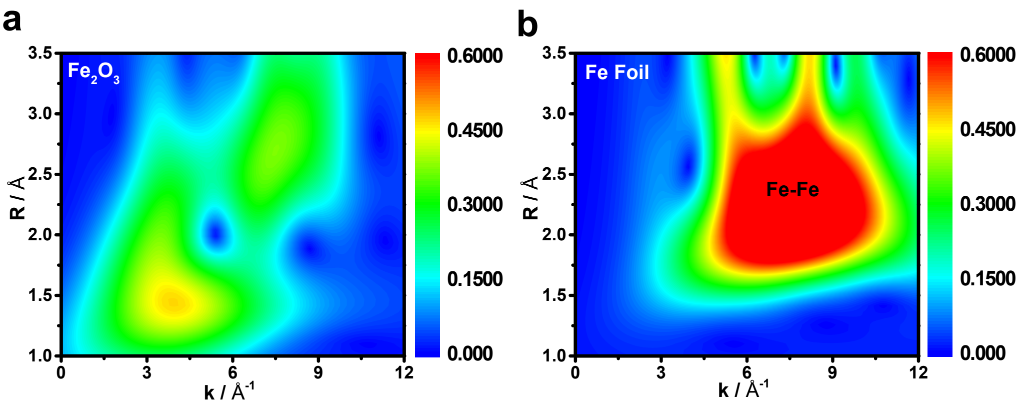

Figure S9. WT-EXAFS spectra on Fe K-edge of (a) Fe_2O_3 and (b) Fe Foil.

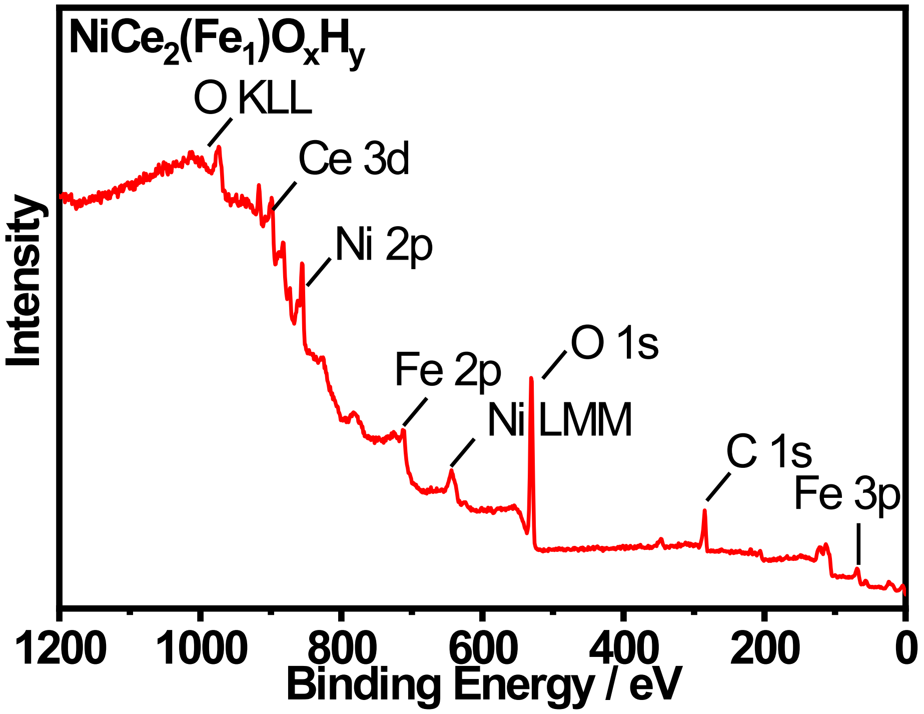

Figure S10. XPS spectrum of $NiCe_2(Fe_1)O_xH_y$ electrode.

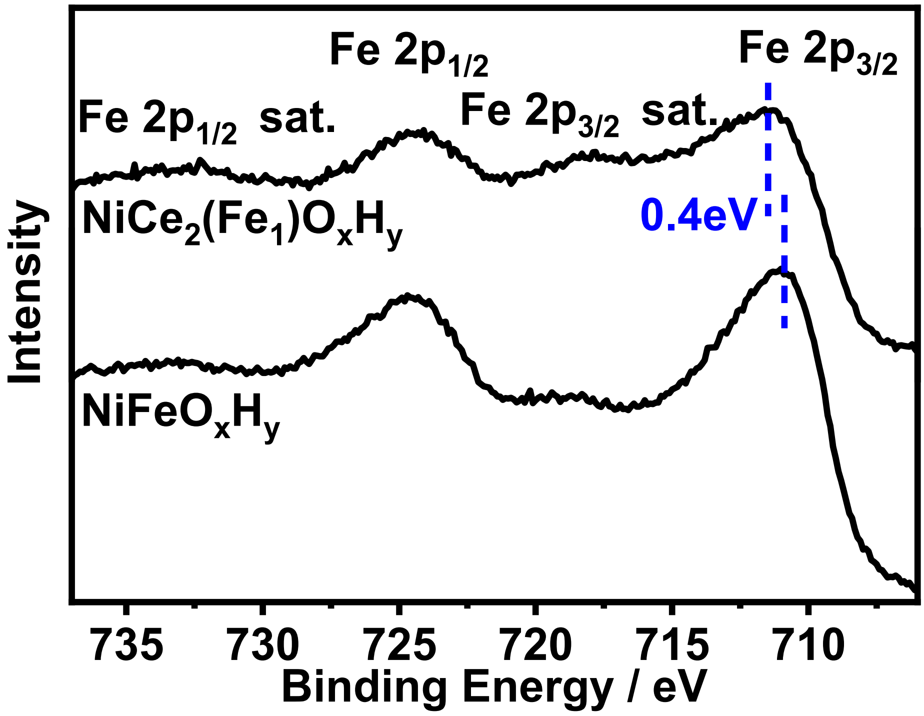

Figure S11. XPS spectra for the Fe 2p regions of the post-OER of NiCe$_2$(Fe$_1$)O$_x$H$_y$ and NiFeO$_x$H$_y$ electrodes.

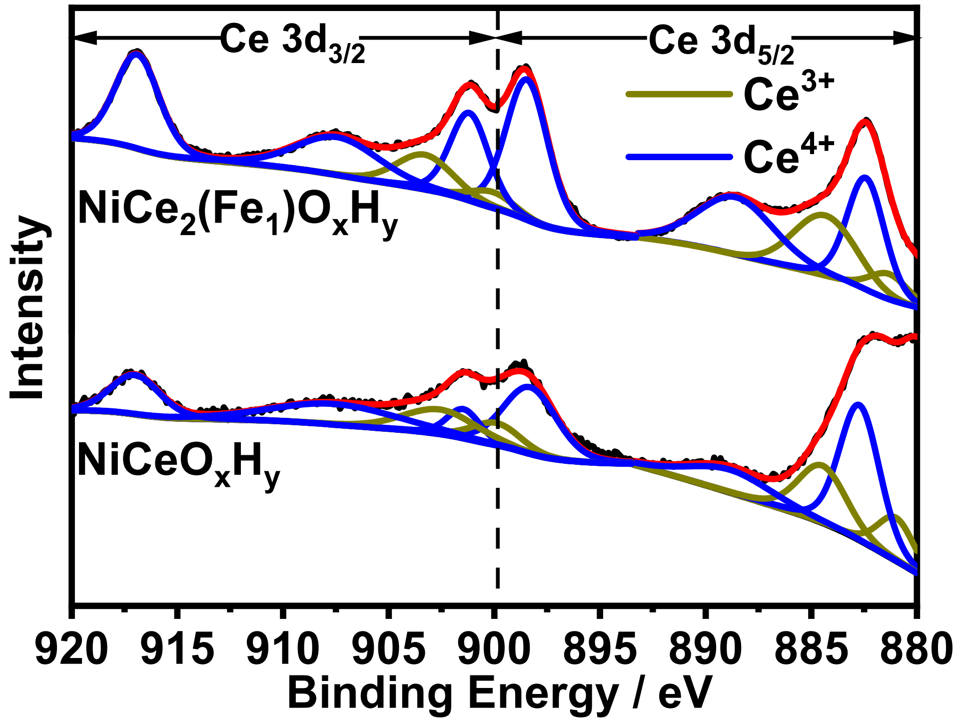

Figure S12. XPS spectra for the Ce 3d regions of the post-OER of NiCe$_2$(Fe$_1$)O$_x$H$_y$ and NiCeO$_x$H$_y$ electrodes.

Table S5. Binding energies and fitting areas for Ce 3d peaks of NiCe$_2$(Fe$_1$)O$_x$H$_y$ in Figure S12.

NiCe$_2$(Fe$_1$)O$_x$H$_y$	Ce^{4+}			Ce^{3+}	
3d$_{3/2}$	u‴	u″	u	u′	u^0
Binding energy/eV	916.9	907.8	901.2	903.4	900.2
Fitting area (a.u.)	25096	19175	20491	11892	4282

Table S6. Binding energies and fitting areas for Ce 3d peaks of $NiCeO_xH_y$ in Figure S12.

$NiCeO_xH_y$	Ce^{4+}			Ce^{3+}	
$3d_{3/2}$	u‴	u″	u	u′	u^0
Binding energy/eV	917.0	908	901.5	902.9	900.0
Fitting area (a.u.)	8795	11671	4365	8224	4916

Table S7. The Ce^{4+}/Ce^{3+} ratios of $NiCe_2(Fe_1)O_xH_y$ and $NiCeO_xH_y$ from the curve-fittings of Ce $3d_{3/2}$ peaks in Figure S12.

	$NiCe_2(Fe_1)O_xH_y$	$NiCeO_xH_y$
Ce^{4+}/Ce^{3+} ratios	4.02	1.89

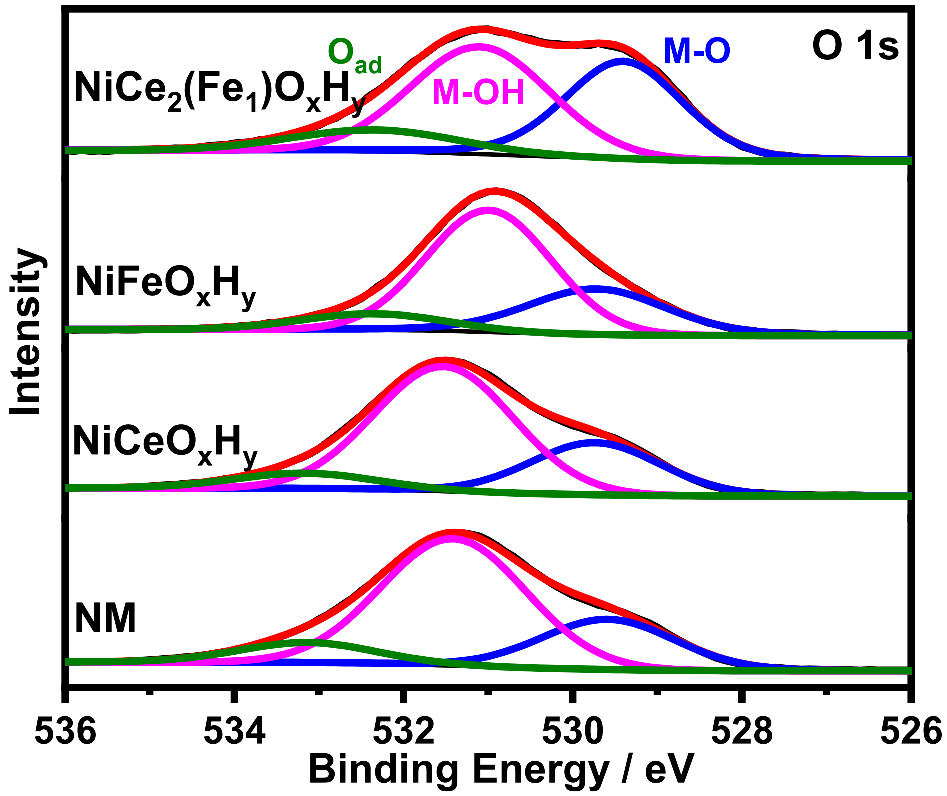

Figure S13. XPS spectra for O 1s regions of the post-OER of $NiCe_2(Fe_1)O_xH_y$, $NiFeO_xH_y$, $NiCeO_xH_y$ and NM electrodes.

Table S8. Binding energies and proportion of M-O species from the O 1s fitted peaks in Figure S13.

Sample	M-O	Ratios of M-O
$NiCe_2(Fe_1)O_xH_y$	529.4	40.12%
$NiFeO_xH_y$	529.7	28.12%
$NiCeO_xH_y$	529.7	26.40%
NM	529.6	24.79%

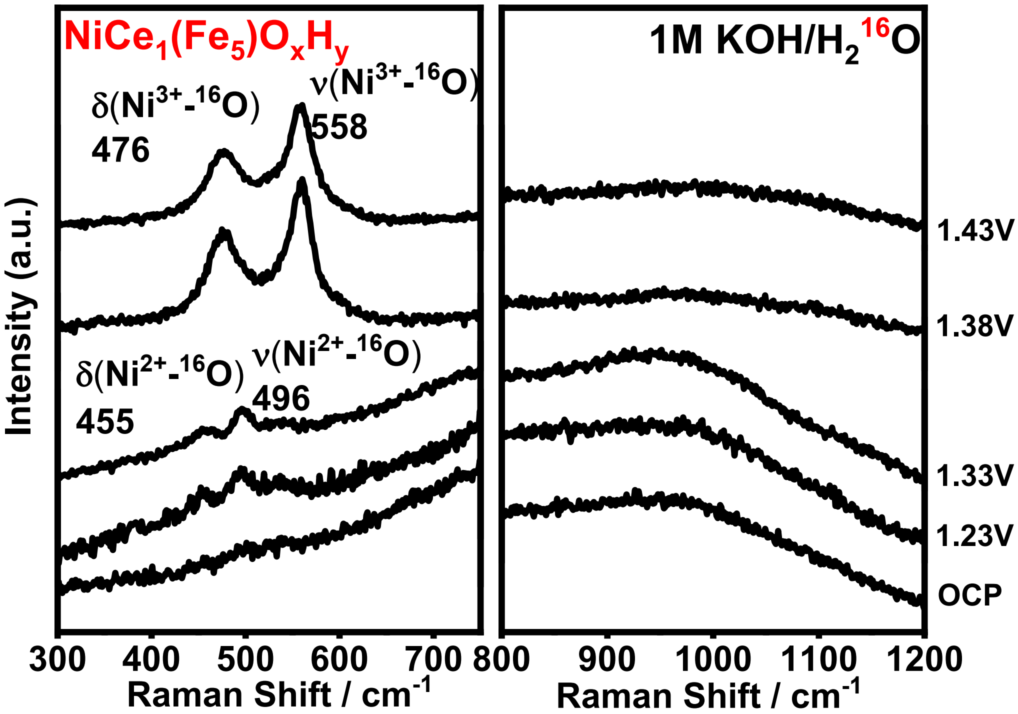

Figure S14. In-situ Raman spectra collected in 1M KOH/$H_2{}^{16}O$ with increasing potential from OCP to OER onset potential of $NiCe_1(Fe_5)O_xH_y$ electrode .

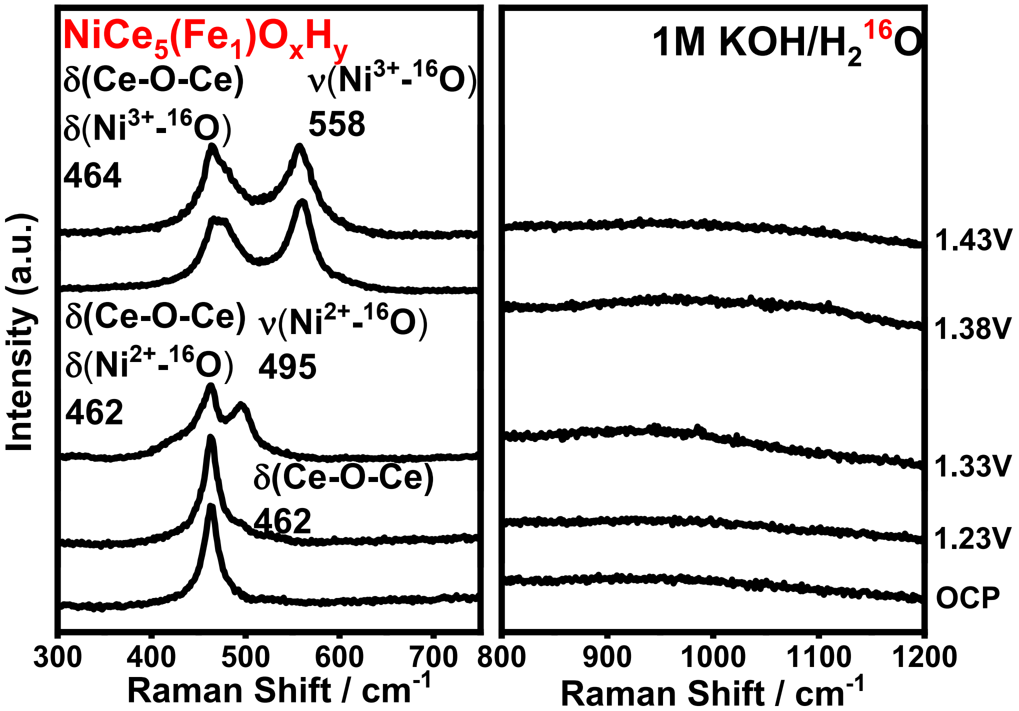

Figure S15. In-situ Raman spectra collected in 1M KOH/$H_2{}^{16}O$ with increasing potential from OCP to OER onset potential of $NiCe_5(Fe_1)O_xH_y$ electrode.

Specially, as for the $NiCe_5(Fe_1)O_xH_y$ electrode, only one peak assigned to Ce-O-Ce binding that located at 462 cm^{-1} was detected before 1.23 V vs. RHE. A new peak located at 495 cm^{-1} at 1.33 V vs. RHE can be assigned as $\nu(Ni^{2+}$-O) while the Ce-O-Ce binding is so strong that it covered the peak related to $\delta(Ni^{2+}$-O), which is the same reason for the missing of $\delta(Ni^{3+}$-O) at higher potential. There was no peak that can be assigned to Fe-O bonding in the recorded spectra.

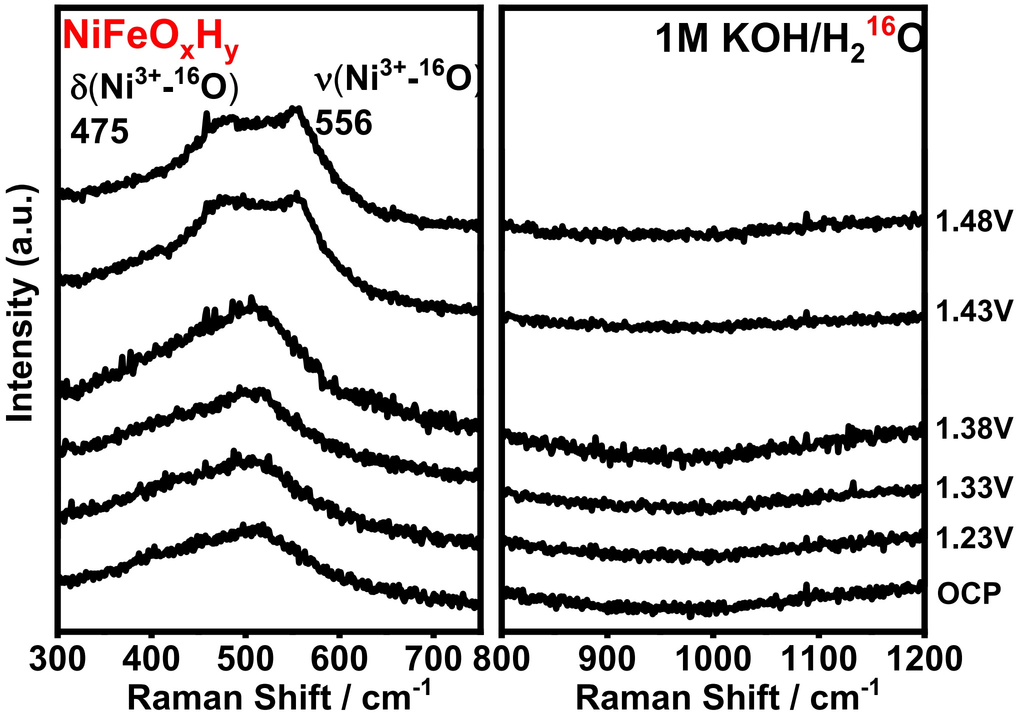

Figure S16. In-situ Raman spectra collected in 1M KOH/$H_2^{16}O$ with increasing potential from OCP to OER onset potential of NiFeO$_x$H$_y$ electrode.

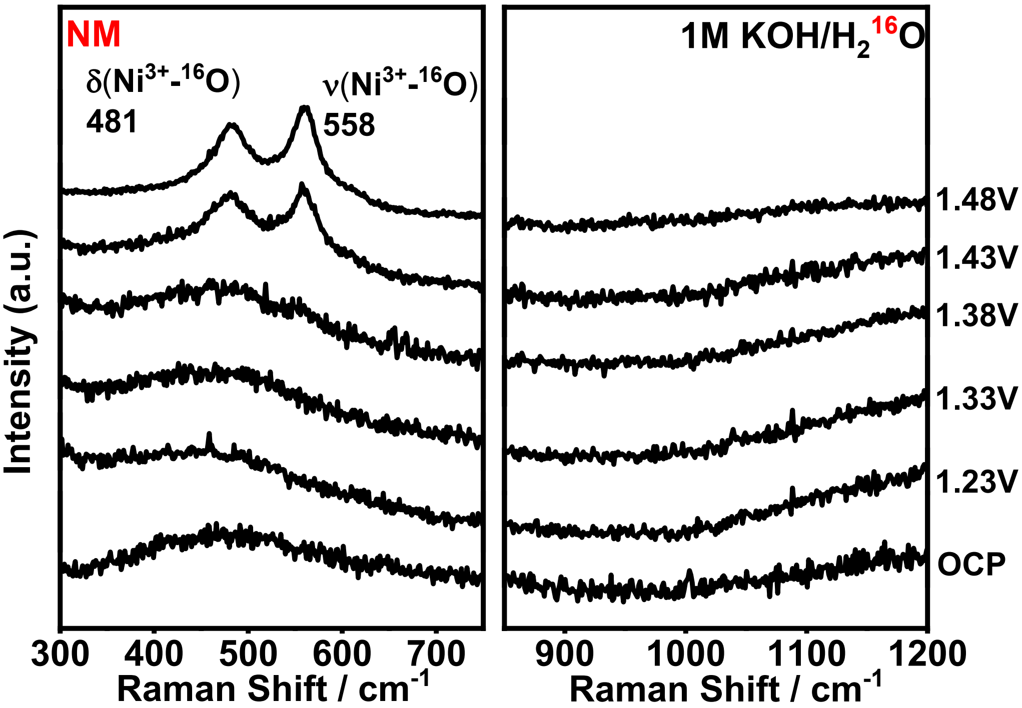

Figure S17. In-situ Raman spectra collected in 1M KOH/$H_2{}^{16}O$ with increasing potentials from OCP to OER onset potential of NM electrode.

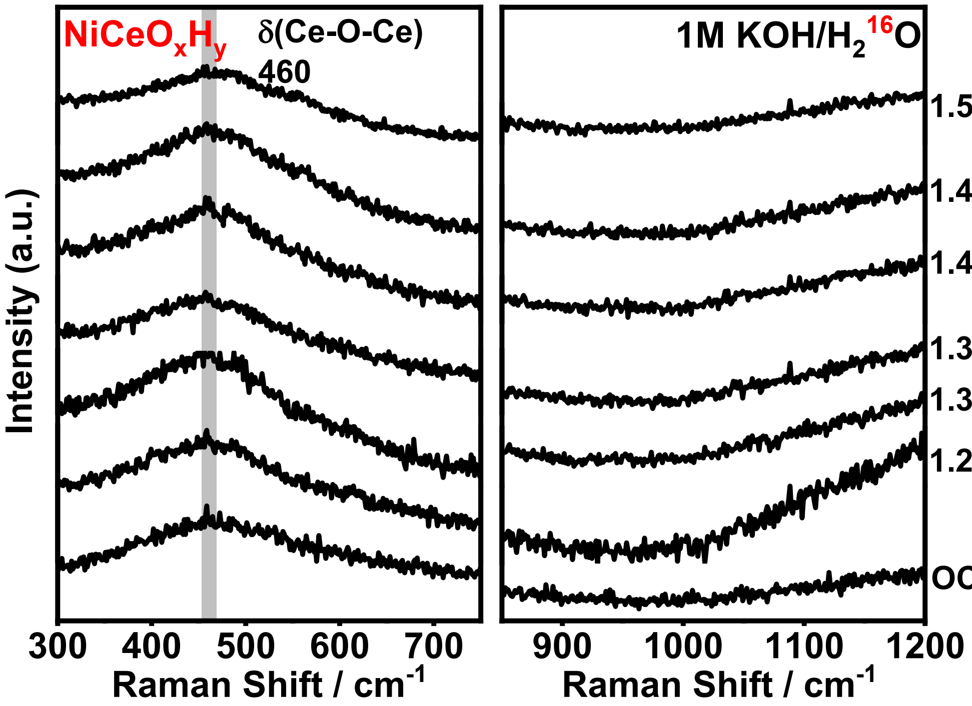

Figure S18. In-situ Raman spectra collected in 1M KOH/$H_2{}^{16}O$ with increasing potentials from OCP to OER onset potential of NiCeO$_x$H$_y$ electrode.

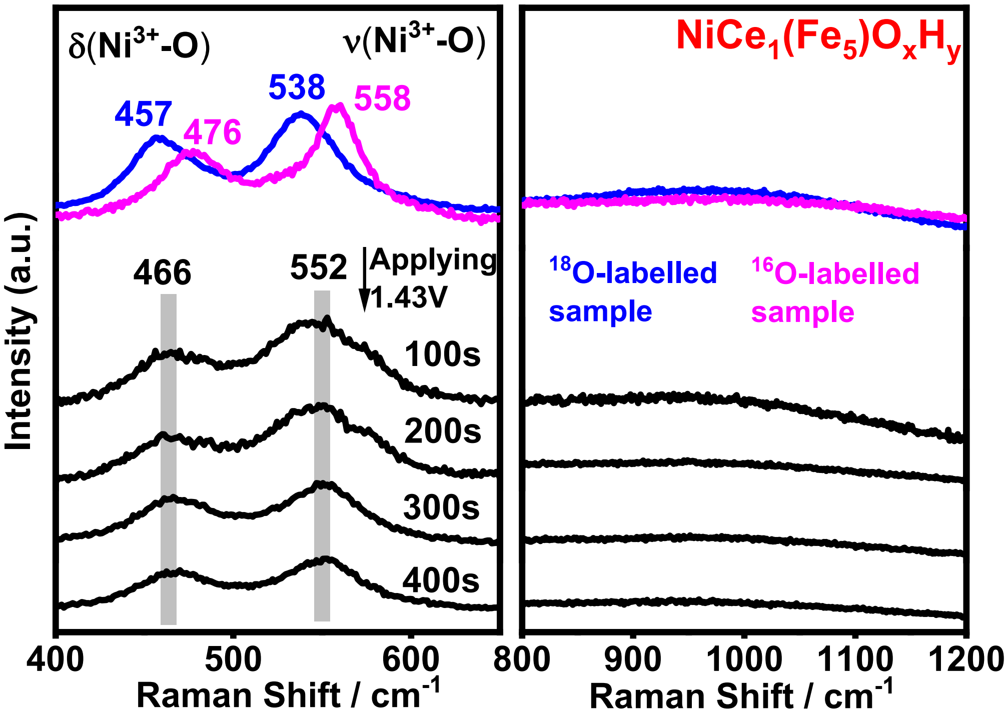

Figure S19. In-situ Raman spectra collected in 1M KOH/$H_2{}^{16}O$ at 1.43V of $NiCe_1(Fe_5)O_xH_y$ electrode after ^{18}O labelling experiment.

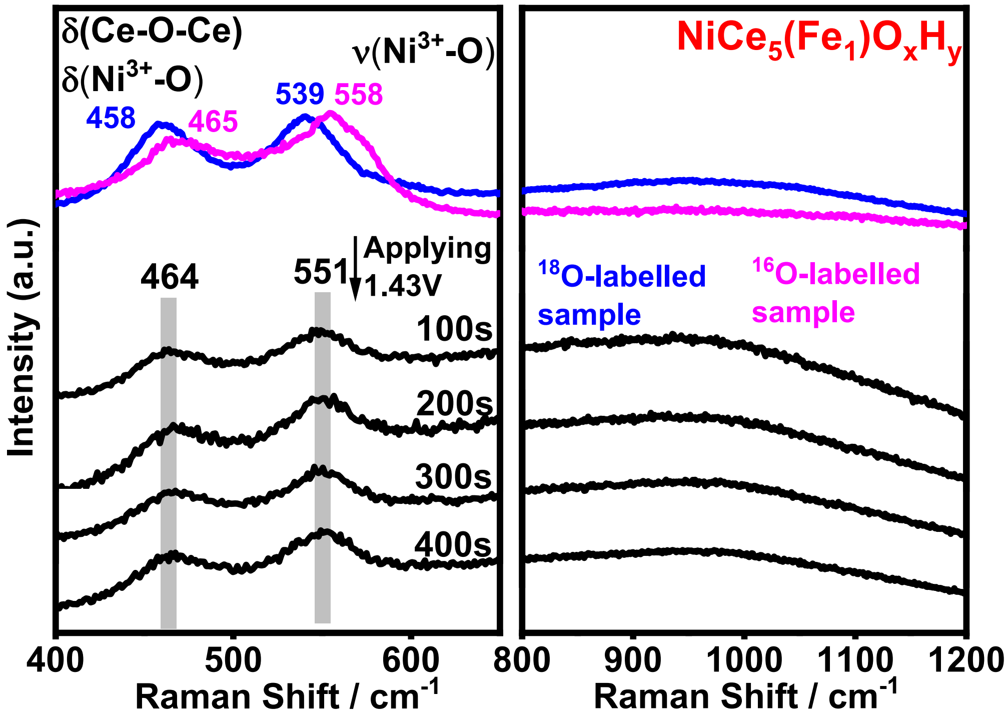

Figure S20. In-situ Raman spectra collected in 1M KOH/$H_2{}^{16}O$ at 1.43V of NiCe$_1$(Fe$_5$)O$_x$H$_y$ electrode after ^{18}O labelling experiment.

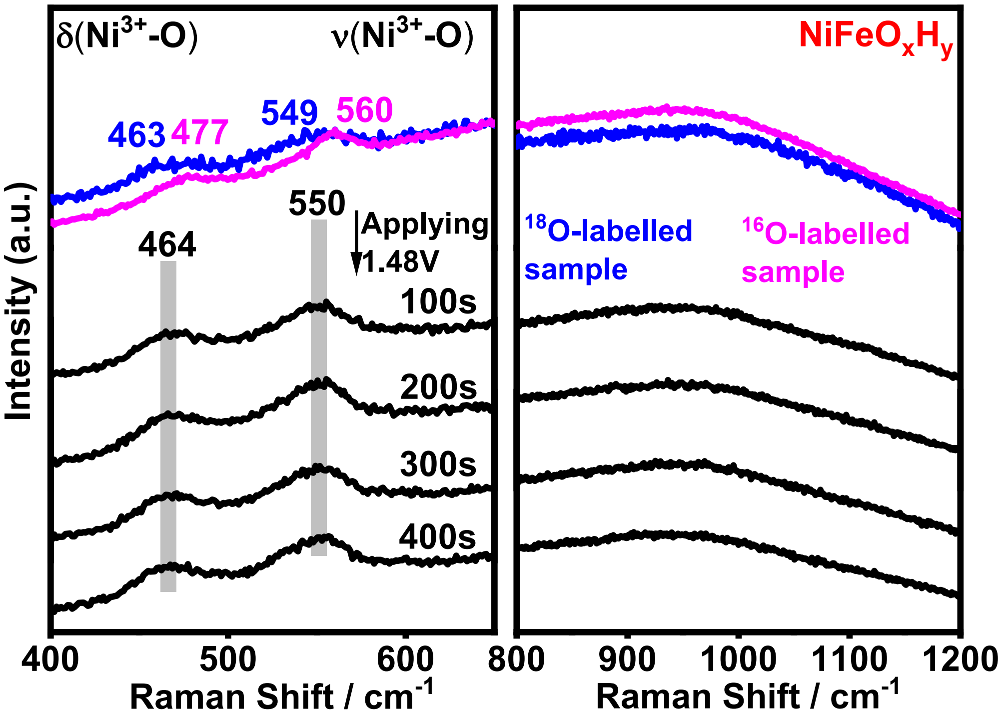

Figure S21. In-situ Raman spectra collected in 1M KOH/$H_2{}^{16}O$ at 1.48V of $NiFeO_xH_y$ electrode after ^{18}O labelling experiment.

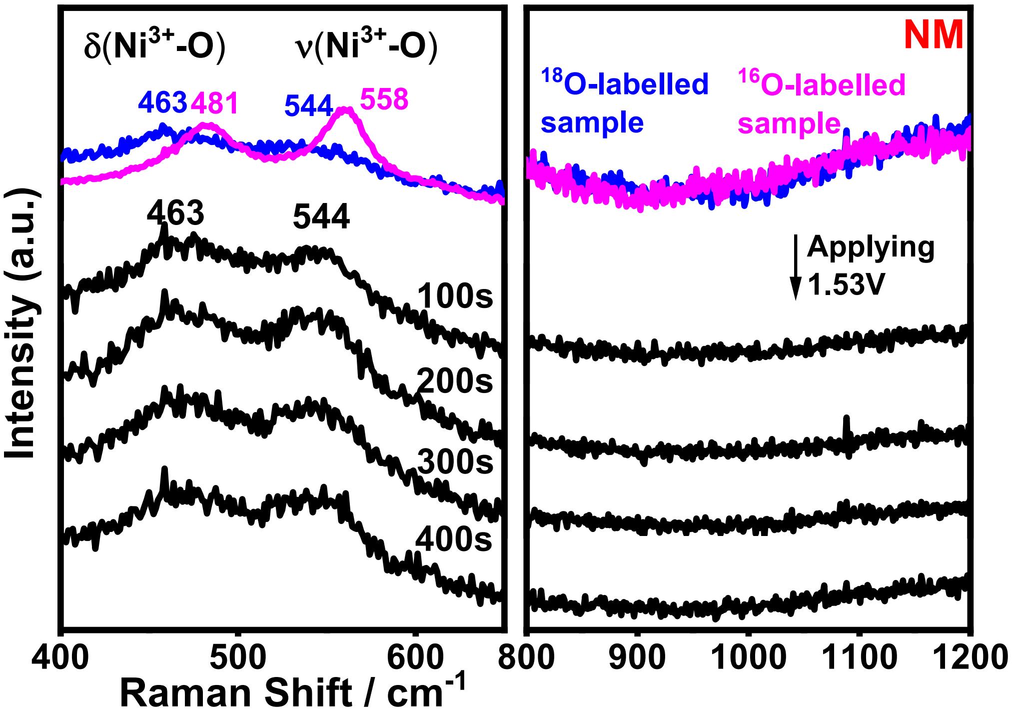

Figure S22. In-situ Raman spectra collected in 1M KOH/$H_2{}^{16}O$ at 1.53V of NM electrode after ^{18}O labelling experiment.

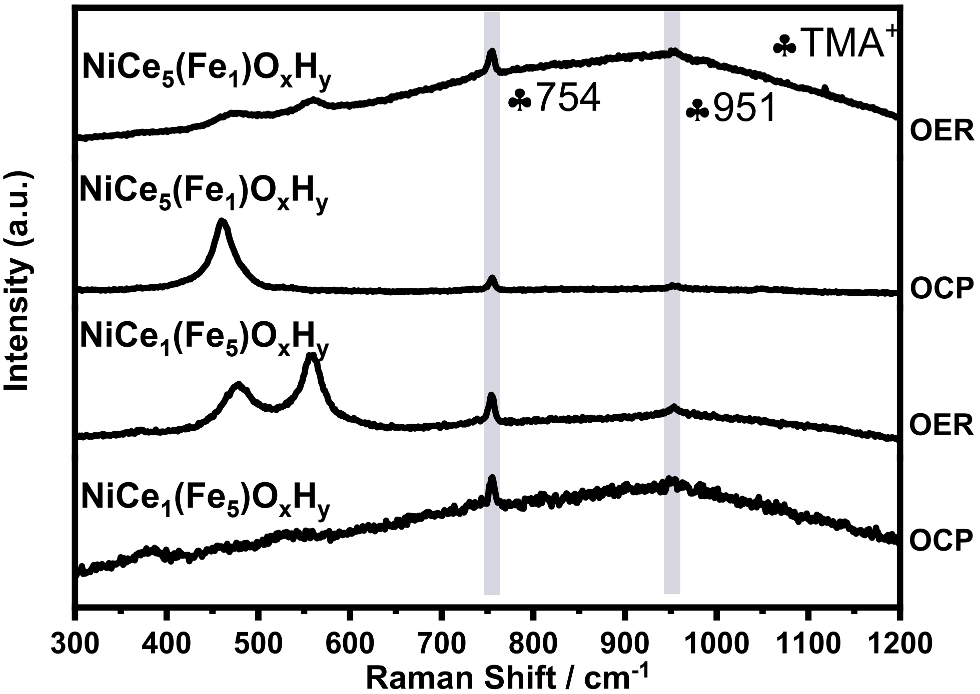

Figure S23. In-situ Raman spectra collected in 1M TMAOH at OCP and OER onset potential of $NiCe_5(Fe_1)O_xH_y$ and $NiCe_1(Fe_5)O_xH_y$ electrodes.

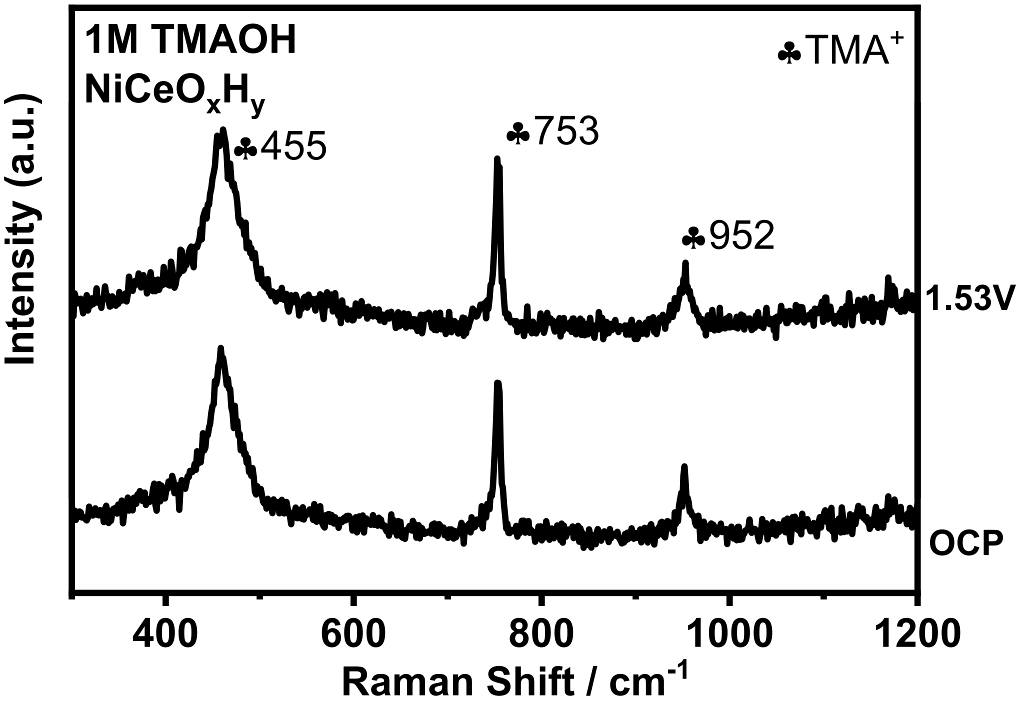

Figure S24. In-situ Raman spectra collected in 1M TMAOH at OCP and OER onset potential of $NiCeO_xH_y$ electrode.

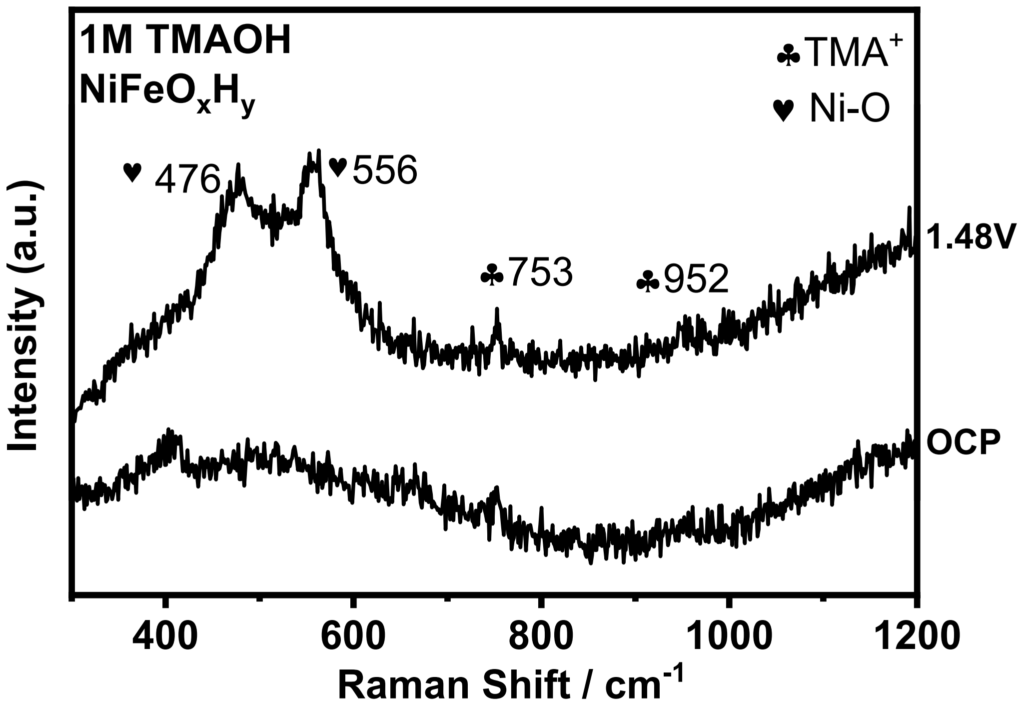

Figure S25. In-situ Raman spectra collected in 1M TMAOH at OCP and OER onset potential of $NiFeO_xH_y$ electrode.

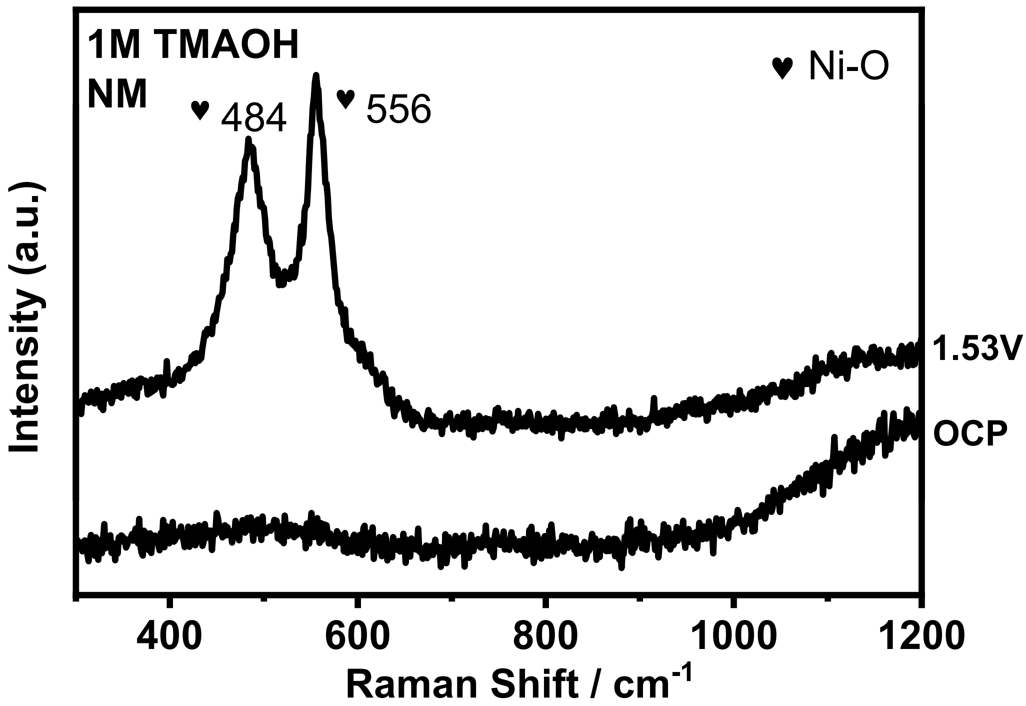

Figure S26. In-situ Raman spectra collected in 1M TMAOH at OCP and OER onset potential of NM electrode.

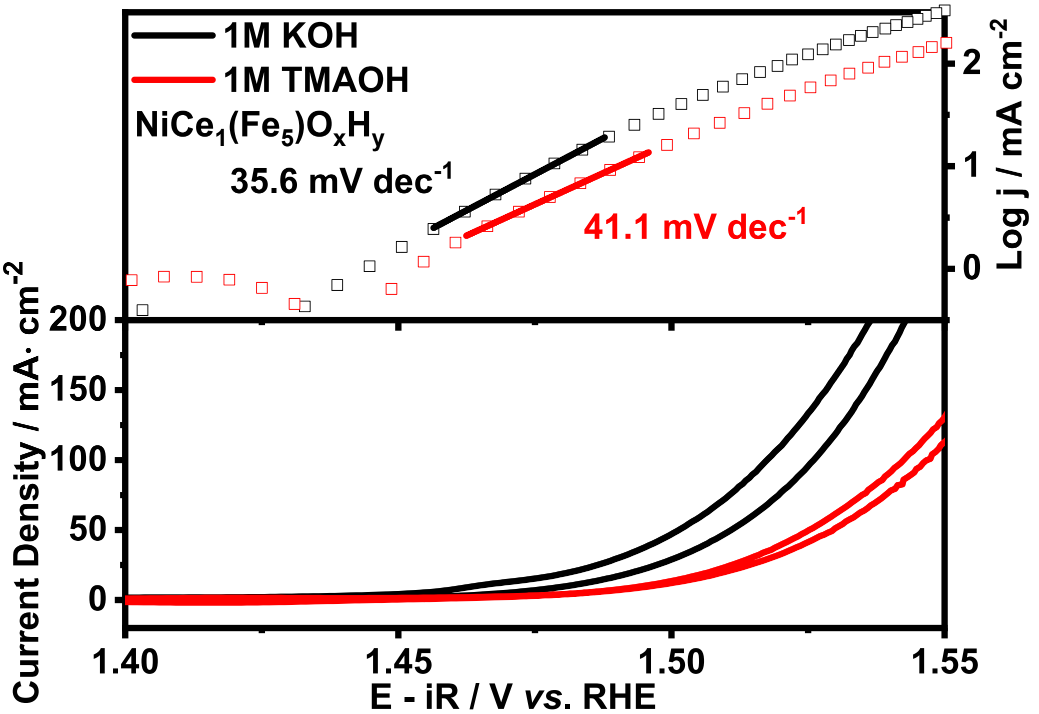

Figure S27. Tafel slopes and polarization curves in 1M KOH and 1M TMAOH of $NiCe_1(Fe_5)O_xH_y$ electrode.

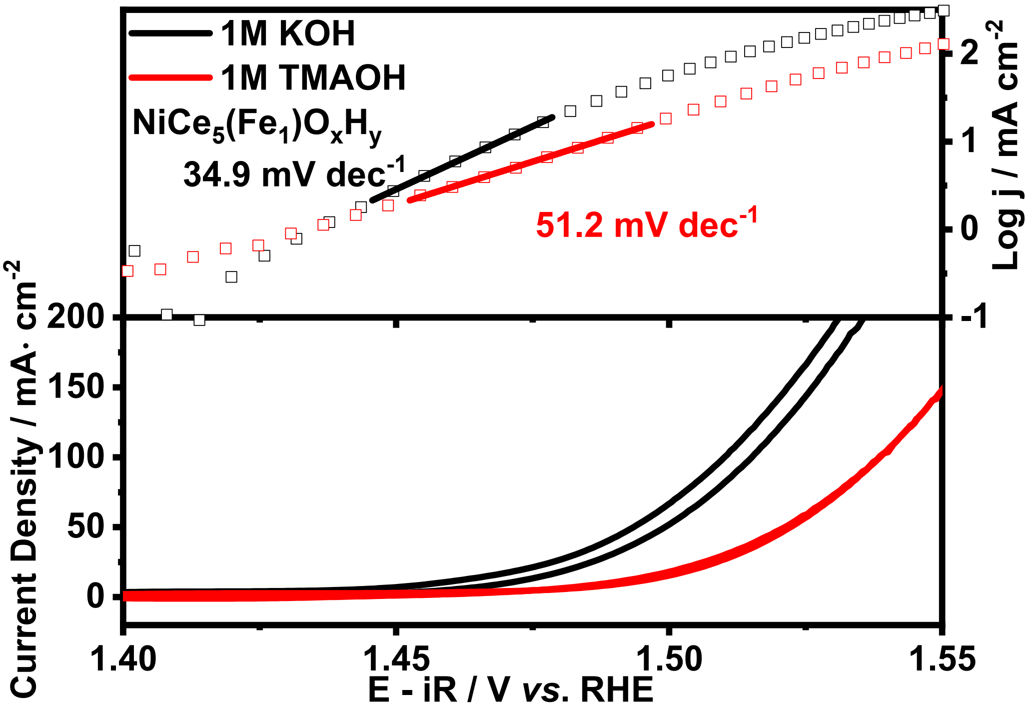

Figure S28. Tafel slopes and polarization curves in 1M KOH and 1M TMAOH of NiCe$_5$(Fe$_1$)O$_x$H$_y$ electrode.

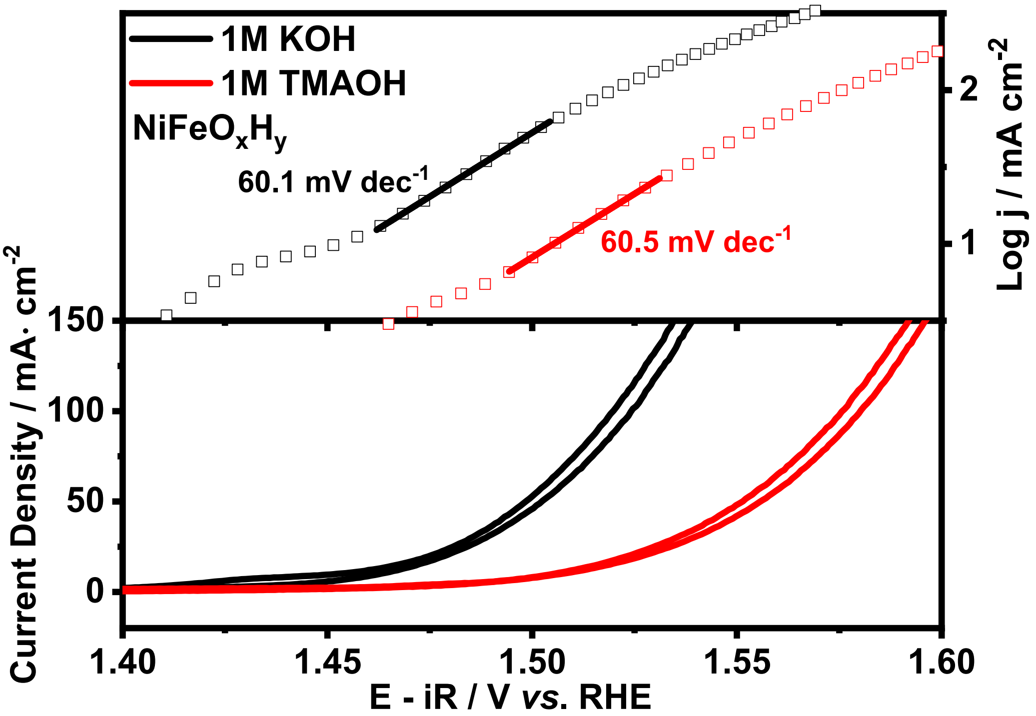

Figure S29. Tafel slopes and polarization curves in 1M KOH and 1M TMAOH of NiFeO$_x$H$_y$ electrode

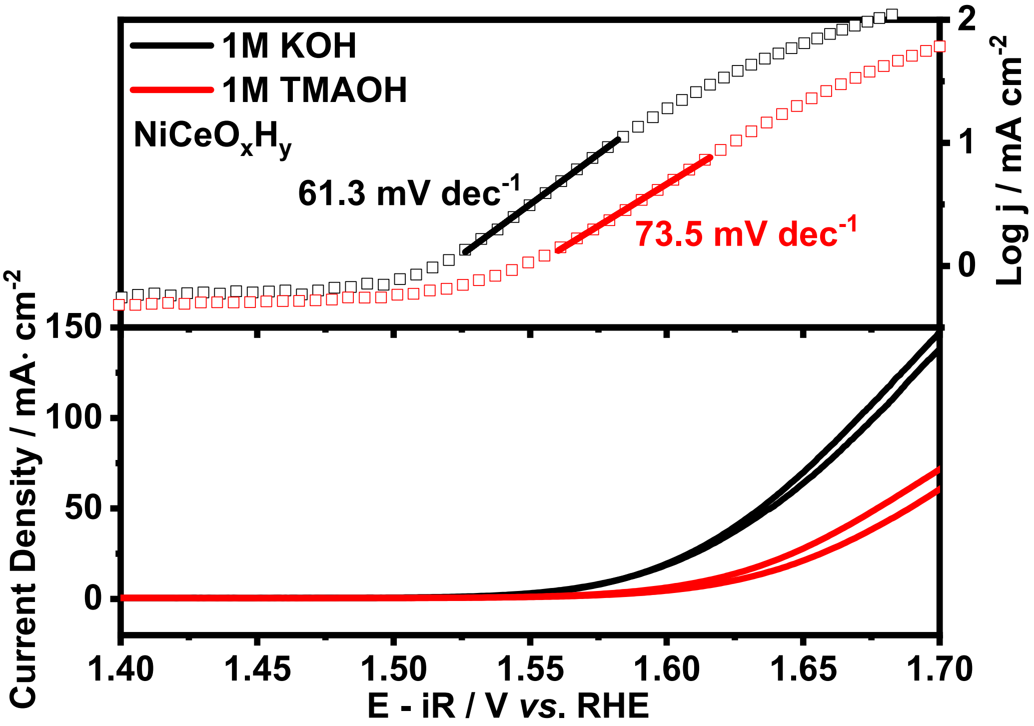

Figure S30. Tafel slopes and polarization curves in 1M KOH and 1M TMAOH of NiCeO$_x$H$_y$ electrode.

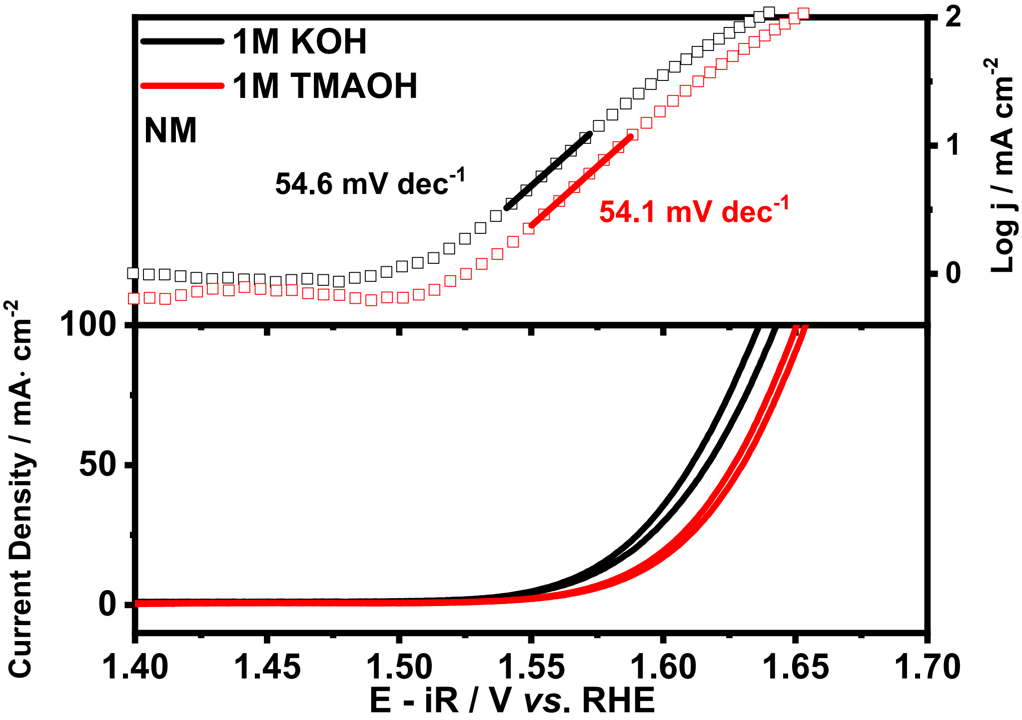

Figure S31. Tafel slopes and polarization curves in 1M KOH and 1M TMAOH of NM electrode.

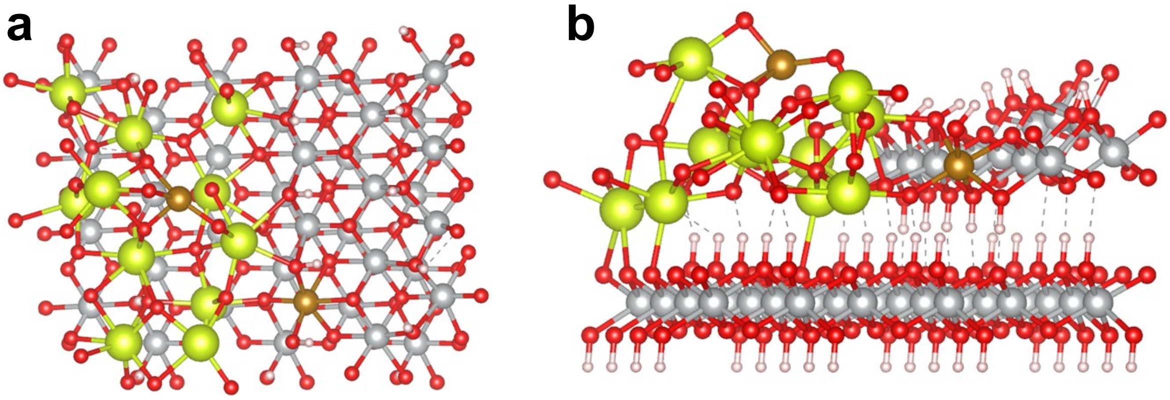

Figure S32. (a) Top and (b) side views of the optimized model of NiCe(Fe)O_xH_y catalysts.

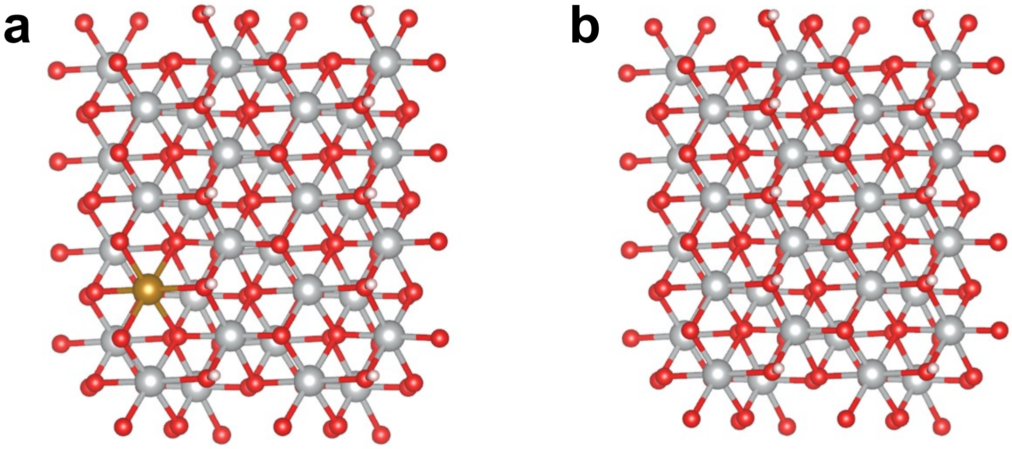

Figure S33. Top views of the optimized models of (a) $NiFeO_xH_y$ and (b) NiO_xH_y catalysts.

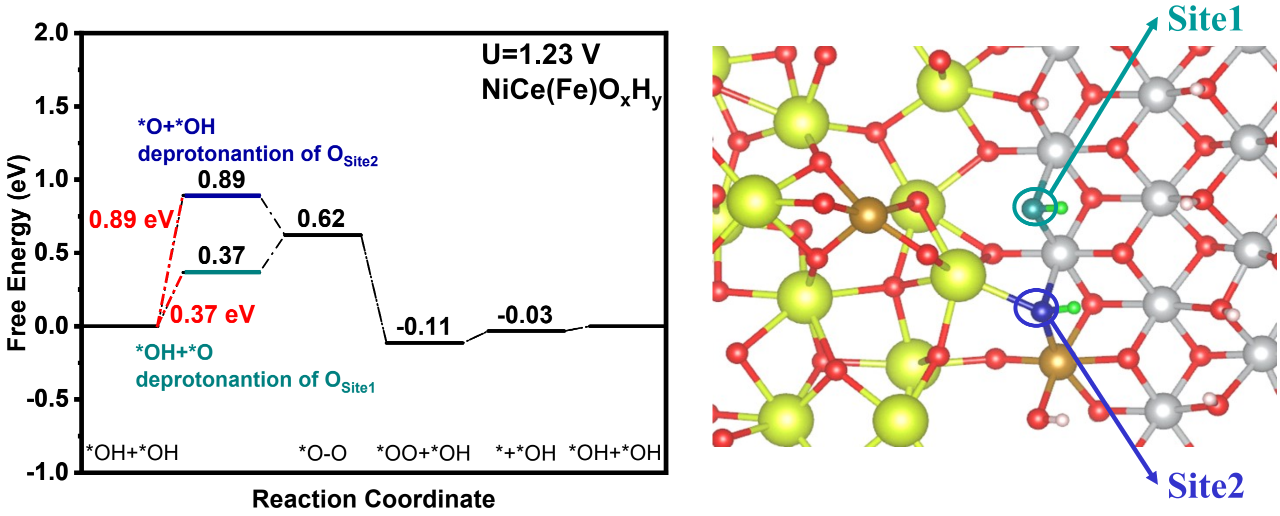

Figure S34. Free energy diagrams of the deprotonation sequence of the two lattice oxygen atom sites and top views of the optimized NiCe(Fe)O_xH_y model.

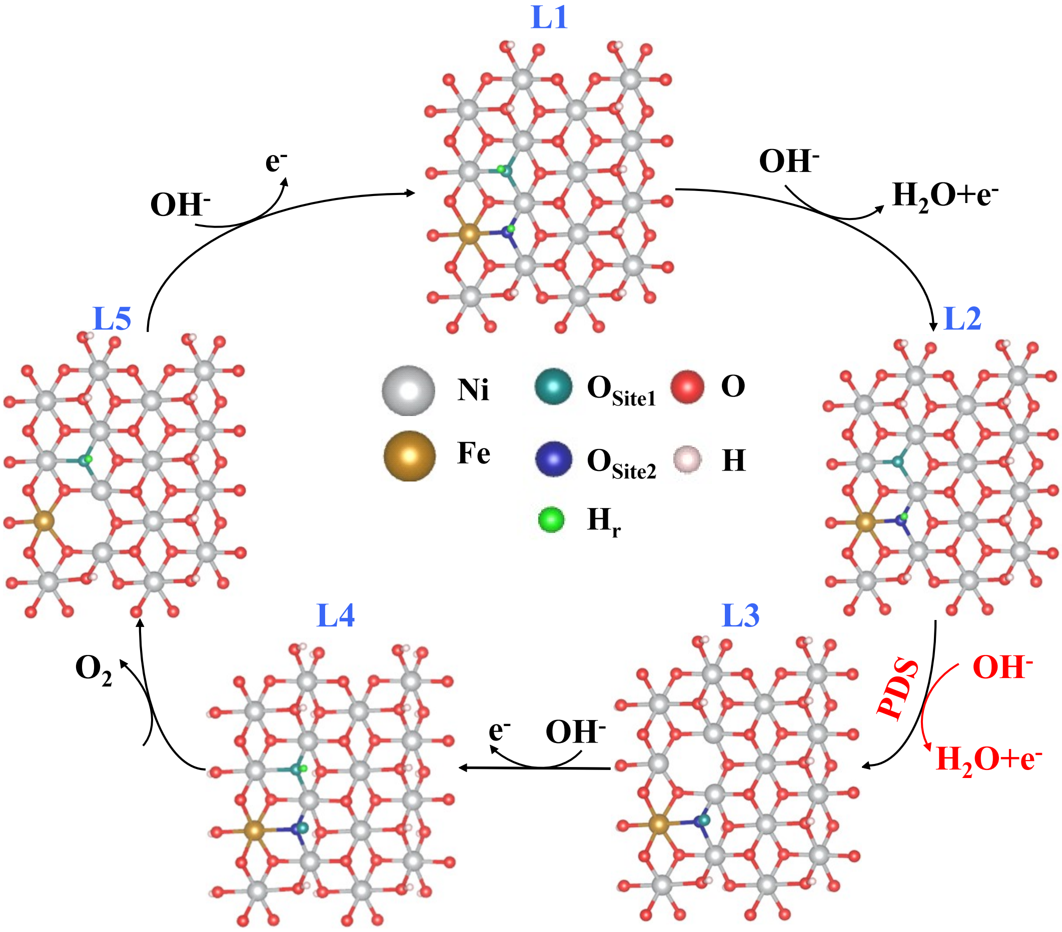

Figure S35. OER cycle of the on optimized $NiFeO_xH_y$ model.

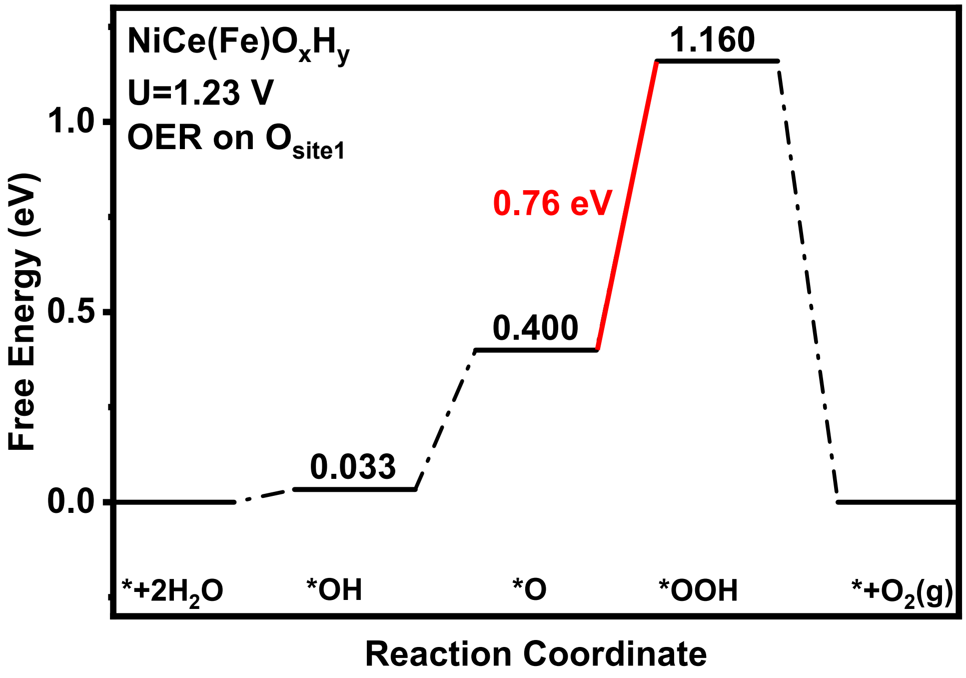

Figure S36. Free energy diagrams of the OER cycle on O_{site1} of NiCe(Fe)O_xH_y.

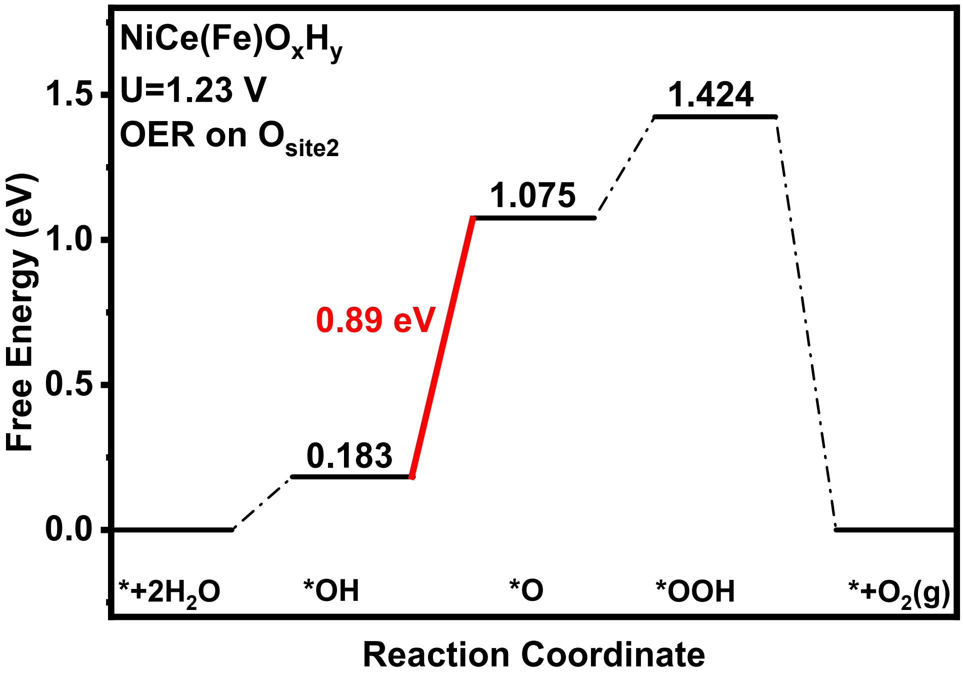

Figure S37. Free energy diagrams of the OER cycle on O_{site2} of NiFeCeO_xH_y.

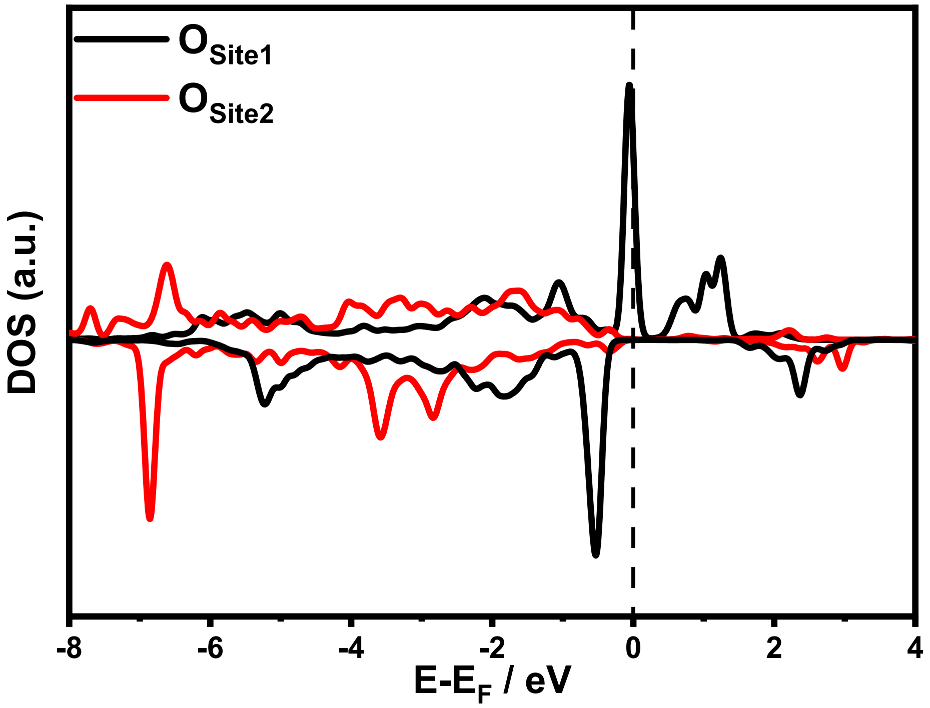

Figure S38. pDOS of O(2p) orbitals of reactive lattice oxygen sites in the L2 intermediates of NiCe(Fe)O_xH_y.

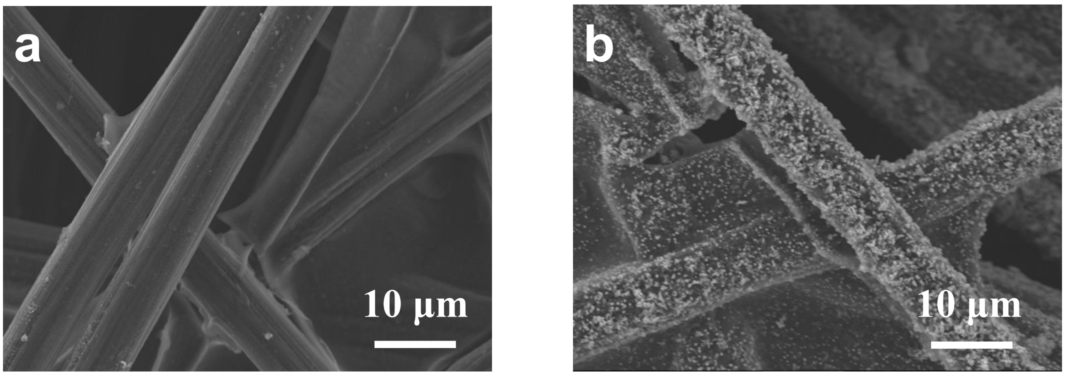

Figure S39. SEM images of cathode coupled with (a) $NiFe_1Ce_2O_xH_y$ and (b) $NiFeO_xH_y$ electrodes after test.

Reference:

1. L. Trotochaud, S. L. Young, J. K. Ranney and S. W. Boettcher, *J Am Chem Soc*, 2014, **136**, 6744-6753.
2. G. Kresse and J. Furthmüller, *Computational Materials Science*, 1996, **6**, 15-50.
3. G. Kresse and J. Furthmuller, *Phys Rev B Condens Matter*, 1996, **54**, 11169-11186.
4. G. Kresse and J. Hafner, *Phys Rev B Condens Matter*, 1993, **47**, 558-561.
5. J. Hafner, *J Comput Chem*, 2008, **29**, 2044-2078.
6. G. Kresse and D. Joubert, *Physical Review B*, 1999, **59**, 1758-1775.
7. P. E. Blochl, *Phys Rev B Condens Matter*, 1994, **50**, 17953-17979.
8. J. P. Perdew, K. Burke and M. Ernzerhof, *Physical Review Letters*, 1997, **78**, 1396-1396.
9. J. P. Perdew, K. Burke and M. Ernzerhof, *Phys Rev Lett*, 1996, **77**, 3865-3868.
10. H. J. Monkhorst and J. D. Pack, *Physical Review B*, 1976, **13**, 5188-5192.
11. S. Grimme, J. Antony, S. Ehrlich and H. Krieg, *J Chem Phys*, 2010, **132**, 154104.